Energy Reports 9 (2023) 1201–1235

Contents lists available at ScienceDirect

Energy Reports

journal homepage: www.elsevier.com/locate/egyr

Research paper

Voltage and frequency regulation in smart grids via a unique Fuzzy PIDD^2 controller optimized by Gradient-Based Optimization algorithm

Kareem M. AboRas [a], Muhammad Ragab [a], Mokhtar Shouran [b,*], Sultan Alghamdi [c,d], Hossam Kotb [a]

[a] Department of Electrical Power and Machines, Faculty of Engineering, Alexandria University, Alexandria 21544, Egypt
[b] Wolfson Centre for Magnetics, School of Engineering, Cardiff University, Cardiff, CF24 3AA, UK
[c] Department of Electrical and Computer Engineering, Faculty of Engineering, King Abdulaziz University, Jeddah, Saudi Arabia
[d] Center of Research Excellence in Renewable Energy and Power Systems, King Abdulaziz University, Jeddah, Saudi Arabia

ARTICLE INFO

Article history:
Received 6 August 2022
Received in revised form 13 November 2022
Accepted 19 December 2022
Available online xxxx

Keywords:
Combined LFC-AVR
PIDD^2 controller
Fuzzy logic control
Renewable energy sources GBO algorithm
Two-area system
ITAE

ABSTRACT

This paper proposes a maiden intelligent controller design that consists of a Fuzzy Proportional–Integral–Derivative–Double Derivative (FPIDD^2) controller whose parameters are fine-tuned using the Gradient-Based Optimization algorithm (GBO). The proposed FPIDD^2 regulator is employed as a secondary regulator for stabilizing the combined voltage and frequency loops in a two-area interconnected power system. It has been shown that the GBO optimization algorithm outperforms other optimization strategies such as the Chimp Optimization Algorithm (ChOA), the Whale Optimization Algorithm (WOA), and the Gorilla Troops Optimization algorithm (GTO). The proposed FPIDD^2 controller is tested in a conventional two-area power system. Then, the investigation is expanded to a two-area hybrid system, with each area comprising a mix of traditional (thermal, gas, and hydraulic power plants) and renewable generation units (wind and solar power). Additionally, the proposed controller takes into account system nonlinearities (such as generation rate limitations, governor deadband, and communication time delays), system uncertainties, and load/renewables fluctuations. In the two tested systems, the dynamic responses of each system demonstrate that FPIDD^2 has a superior ability to attenuate the deviations in voltage and frequency in both areas of the system. In the studied conventional system, the proposed FPIDD^2 controller is compared with a PID controller tuned by the Multi-Objective Non-Linear Threshold Accepting Algorithm (MONLTA), which has been presented in the literature, and a Fuzzy PID (FPID) controller tuned by GBO. In the investigated hybrid system, the suggested FPIDD^2 regulator is compared to a GBO-tuned Integral Derivative-Tilted (ID-T) controller and FPID controller. As a fitness function (FF) for the GBO, the criteria of minimizing the integral time absolute error (ITAE) are applied. The results are presented in the form of MATLAB/SIMULINK time-domain simulations.

1. Introduction

The simultaneous management of a synchronous generator's terminal voltage and area frequency can be considered one of the major hurdles that the engineering world encounters in the field of electrical power systems. The degradation of any of these characteristics has a tremendous effect on the life expectancy and performance of other power systems' operational equipment. Small load disruptions are dealt with by controlling devices placed in big complex power systems in order to maintain system voltage and frequency within defined limits. The generating power plants are always equipped with two operational loops in this regard. One of these loops is the load frequency control (LFC) loop, which regulates the frequency by lowering the gap between real power generation and load. The other is the automatic voltage regulator (AVR) loop, which is responsible for managing the system's reactive power and, as a result, the terminal voltage (Kalyan and Rao, 2021a). The combined AVR-LFC systems are required to assist the inter-area power generating systems' dependability, security, and performance. It has been demonstrated that certain interactions between the AVR loop and the LFC loop occur in response to dynamic perturbations (Saadat, 2011). This is because the AVR loops have a direct impact on the magnitude of the power generation voltage (Bingul and Karahan, 2018).

Fosha and Elgerd (1970) performed groundbreaking research in the area of LFC for power grid networks. Since that day, a large

* Corresponding author.
E-mail addresses: kareem.aboras@alexu.edu.eg (K.M. AboRas), Muhammad.ragab@alexu.edu.eg (M. Ragab), shouranma@cardiff.ac.uk (M. Shouran), smalgamdi1@kau.edu.sa (S. Alghamdi), hossam.kotb@alexu.edu.eg (H. Kotb).

https://doi.org/10.1016/j.egyr.2022.12.054
2352-4847/

Nomenclature

GBO	Gradient-Based Optimization
ChOA	Chimp Optimization Algorithm
WOA	Whale Optimization Algorithm
GTO	Gorilla Troops Optimization
MONLTA	Multi-Objective Non-Linear Threshold Accepting Algorithm
PID	Proportional–Integral–Derivative
PIDD^2	Proportional–Integral–Derivative–Double Derivative
ID-T	Integral Derivative-Tilted
FPID	Fuzzy Proportional–Integral–Derivative
FPIDD^2	Fuzzy Proportional–Integral–Derivative –Double Derivative
LFC	Load Frequency Control
AVR	Automatic Voltage Regulator
PV	Photovoltaics
RESs	Renewable energy sources
A_T	The rotor-swept area (m^2)
β	The pitch angle
C_P	The power coefficient of the rotor blades
V_W	The rated wind speed (m/s)
r_T	The rotor radius
λ	The tip-speed ratio (TSR)
λ_I	The intermittent TSR
ρ	Air density (kg/m^3)
P_W	The wind turbine output power (W)
FO	Fractional Order
FOC	FO Calculus
FOPID	Fractional Order Proportional Integral Derivative
GDB	Governor Dead Band
GRC	Generation Rate Constraint, % (p.u)
LEO	Local Escaping Operator
GSR	Gradient Search Rule
DM	Direction of Movement
m	The current iteration
M	The maximum number of iterations
N	Population size
ITAE	Integral time absolute error
T_{sim}	Simulation time
CTD	Communication Time Delay
SLP	Step Load Perturbation
MSLP	Multi-Step Load Perturbation
RLP	Random Load Perturbation
M_p	Maximum overshoot magnitude of terminal voltage
τ_s	Settling time of the terminal voltage
τ_r	Rise time of the terminal voltage
τ_p	Peak time of the terminal voltage
MO	Maximum Overshoot of deviations in frequency and tie-line power
MU	Maximum Undershoot of deviations in frequency and tie-line power
ST	Settling Time of deviations in frequency and tie-line power
C_{12}	Synchronization coefficient
$V_{out.1}$	The output terminal voltage of area-1 (p.u)
$V_{out.2}$	The output terminal voltage of area-2 (p.u)
ΔF_1	The frequency deviation in Area 1 (Hz)
ΔF_2	The frequency deviation in Area 2 (Hz)
ΔP_{tie}	The tie-line power deviation (p.u)
K_P	Proportional gain of the PIDD^2 controller
K_I	Integral gain of the PIDD^2 controller
K_{D1}, K_{D2}	Derivative gains of the PIDD^2 controller
N_1, N_2	The coefficients of the filters
K_T	Tilted gain of the ID-T controller
n	Fractional component of the ID-T controller
K_1, K_2	Scaling factors of the fuzzy controller inputs

body of literature in this field has been produced, some of which is presented in this paper. Regarding the stability evaluation of a nuclear power station, Dhanasekaran et al. (2020) proposed a classical PID regulator with multiple objective functions based on an ant colony optimizer (ACO). Traditional PI (Mohanty and Hota, 2018; Dhillon et al., 2016)/PID (Guha et al., 2016; Madasu et al., 2018; Hakimuddin et al., 2020; Barisal and Mishra, 2018; Rao, 2020)/PIDD^2 (Kalyan and Suresh, 2021) controllers have been extensively used for many types of power systems with multiple areas due to their ease of implementation. In addition, the authors used the Chemical Reaction-based Particle Swarm Optimizer (CRPSO) (Mohanty and Hota, 2018), hybrid Bacterial Foraging-Particle Swarm Optimizer (BFOA-PSO) (Dhillon et al., 2016), Grey Wolf Optimizer (GWO) (Guha et al., 2016), Flower Pollination Algorithm (FPA) (Madasu et al., 2018), Genetic Algorithm (GA) (Hakimuddin et al., 2020), Improved Particle Swarm Optimizer (IPSO) (Barisal and Mishra, 2018), Differential Evolution (DE) (Rao, 2020), and Grey Wolf Optimizer (GWO) (Kalyan and Suresh, 2021). The authors in Mohanty and Hota (2018), Guha et al. (2016) and Madasu et al. (2018) investigated a two-area system containing hydro-thermal producing units, while the authors in Hakimuddin et al. (2020), Barisal and Mishra (2018), Rao (2020) and Kalyan and Suresh (2021) worked on a multi-area interconnected power system containing also conventional units such as thermal, hydro and gas units. Furthermore, because controllers provide extra optimizing parameters in fractional order (FO), they are gaining popularity, particularly in LFC schemes, and are largely approved by academics (Tungadio and Sun, 2019). Also, from the FOCs family, a tilt integral derivative (TID) controller has recently been employed to overcome LFC difficulties. As a result, various research (Topno and Chanana, 2018; Elmelegi et al., 2021) recommended the TID controller as a solution to LFC difficulties. Ahmed et al. (2022) proposed a modified version of TID called ID-T whose parameters are fine-tuned by Archimedes optimization algorithm (AOA). The particle swarm optimizer (PSO) (Al-Hinai et al., 2021), Firefly Algorithm combined with Pattern Search (FAPS) (Rajesh et al., 2019), Wild Horse Optimizer (WHO) (Khudhair et al., 2022), Imperialist Competitive Algorithm (ICA) (Yogendra, 2018), and others have been used in previous studies. The authors in the above-mentioned papers focused primarily on system frequency stabilization, focusing solely on the LFC problem and ignoring the AVR coupling. Separately, there is a vast number of studies on LFC and

AVR. Researchers are now focusing on doing work with integrated LFC-AVR models; however, they are limited in some ways. By inserting a damper winding into the synchronous generator rotor of the AVR loop, Ref. Gupta et al. (2014) examined a combined LFC-AVR model and studied the controlled response, although the research was restricted to one area. A combined LFC-AVR study of a standalone thermal power unit controlled by a proportional–integral (PI) controller is shown in Ref. Rakhshani et al. (2009). Ref. Vijaya Chandrakala and Balamurugan (2016) applied an LFC-AVR combination study to the multi-regional systems with conventional hydrothermal power plants, all under the assistance of classic PID control based on Simulated Annealing (SA). The authors of Rajbongshi and Saikia (2017a) investigated the application of coupled LFC-AVR model to a system consisting of three areas controlled by an F-based regulator well-tuned using the Lightning Search Algorithm (LSA), however only diesel and thermal power plants were inserted in each respective area. The authors in Refs. Lal and Barisal (2019) and Kalyan and Rao (2021b) used a multi-area system involving various generating power plants in their study of LFC-AVR combination, even though the study was confined to the use of traditional PID utilizing the Moth Flame Optimization technique (MFO) (Lal and Barisal, 2019) and the hybrid Differential Evolution-Artificial Electric Field Algorithm (DE-AEFA) (Kalyan and Rao, 2021b), respectively. Authors in Gupta et al. (2016) presented a hybrid controller that utilizes the benefits of neural networks and rapid traversal filters in order to investigate the interaction between the LFC loop and AVR loop in a one-area power system. For a two-area power system, Ref. Shyama et al. (2012) introduces an AVR-LFC solution that relies on a Fuzzy Gain Scheduled Proportional–Integral (FGSPI) structure. This method surpassed a traditional Proportional–Integral (PI) controller in a comparison that employed many performance metrics. When considering convergence stability, implementation simplicity, and computing efficacy, the FGSPI technique outperformed the others. The PID controller parameters of an AVR-LFC combination of a one-area power system are determined using a Particle Swarm Optimization (PSO) approach in Soundarrajan et al. (2010). Refs. Morsali and Esmaeili (2020), Rajbongshi and Saikia (2019), Rajbongshi et al. (2018) and Kalyan et al. (2022) introduces more research inquiries into the connection between the AVR-LFC regulatory methods. Regardless of the diversity of PID control systems, the performance and robustness of such solutions were tested by the uncertainties in the dynamics of the power production units.

Some recent research studies have focused on customizing and developing unique optimization processes that can survive large levels of uncertainty in dynamical parameters and consequently obtain superior results (Nahas et al., 2019; Nahas and Nourelfath, 2014; Nahas et al., 2021). In Refs. Nahas and Nourelfath (2014), Nahas et al. (2021), Ekinci and Hekimoğlu (2019) and Ranjan et al. (2021) heuristics such as the Nonlinear Threshold Accepting Algorithm (NLTA), Multi-Objective Nonlinear Threshold Accepting Algorithm (MONLTA), improved kidney-inspired algorithm (IKA), and Mine Blast Algorithm (MBA) have been developed to enhance the settings of Proportional–Integral–Derivative (PID) controller For AVR control systems. Refs. Chatterjee and Mukherjee (2016), Ortiz-Quisbert et al. (2018) and Modabbernia et al. (2020) proposes other ways relied on a teaching–learning controller, fractional-order PID regulator, and H∞ control strategy with μ-analysis. For multi-area interconnected power systems, the problem at hand includes interacting loops of AVR-LFC regulators. For individual AVR or LFC, typical solutions are implemented using either analytical or heuristic techniques. These, on the other hand, do not strike a balance between competing objectives (e.g., regulating voltage to the desired level or regulating frequency owing to load changes), nor do they handle the physical interconnectivity between the various power system areas (Kumar et al., 2021).

This inspired the developers of this study to construct a newly smart-based fuzzy PIDD^2 regulator for an LFC-AVR combination model for a dual-area system containing numerous conventional and renewable generating units in order to concurrently stabilize voltage and frequency. Until recently, writers have solely concentrated on the installation of conventional and FO-based controllers in the LFC-AVR combined analysis stream. Because the combined LFC-AVR system is more sophisticated, Standard controllers cannot be used anymore, particularly for strong disturbances. In both the LFC and AVR loops, fuzzy PIDD^2 fine-tuned using the GBO algorithm was used as a secondary regulatory strategy.

1.1. Contribution of the paper

This research offers an intelligent-based fuzzy PIDD^2 controller for frequency and voltage stability in various systems (i.e., conventional and hybrid) with significant RESs penetration, considering a variety of load patterns, system uncertainties, and nonlinearities. The major contributions of the work are described as follows concerning the latest research on related threads:

(a) The proposal of a maiden robust controller combining the benefits of fuzzy and PIDD^2 controllers (FPIDD^2) for simultaneous voltage and frequency stabilization of conventional and hybrid two-area interconnected power systems.
(b) The use of the innovative and efficient optimization approach GBO to determine the finest settings of the presented controller.
(c) Comparisons to the performance of other, more sophisticated algorithms (such as ChOA Khishe and Mosavi, 2020, WOA Mirjalili and Lewis, 2016, and GTO Abdollahzadeh et al., 2021) are used to prove the GBO's superiority.
(d) To analyze the system stability status, multiple problems were taken into account, including the significant penetration of RESs in both areas, various load perturbation patterns, communication time delay, and time-varying desired output voltage.
(e) The superiority of fuzzy PIDD^2 was demonstrated through performance comparisons with classic PID (Nahas et al., 2021), ID-T (Ahmed et al., 2022), and intelligent fuzzy PID (Tasnin and Saikia, 2018) controllers.
(f) The consideration of many different cases, such as tuning an isolated LFC and AVR systems, and tuning the combined LFC-AVR system.

The following is how the rest of the paper is structured: The architecture of the investigated systems is shown in Section 2. The suggested controller structure and the optimization utilized for tuning its parameters are presented in Section 3, while Section 4 shows the results of the simulation for conventional and hybrid systems with different cases and their discussion. The paper's conclusion is found in Section 5.

2. Investigated system modeling

The proposed controller is tested on two systems: a basic conventional two-area power system and a hybrid system, which are described in detail in the following subsections.

2.1. The configuration of the conventional power system

The power system shown in Fig. 1 consists of two areas with equal generation capacity. Fig. 1 shows in a simple form how the

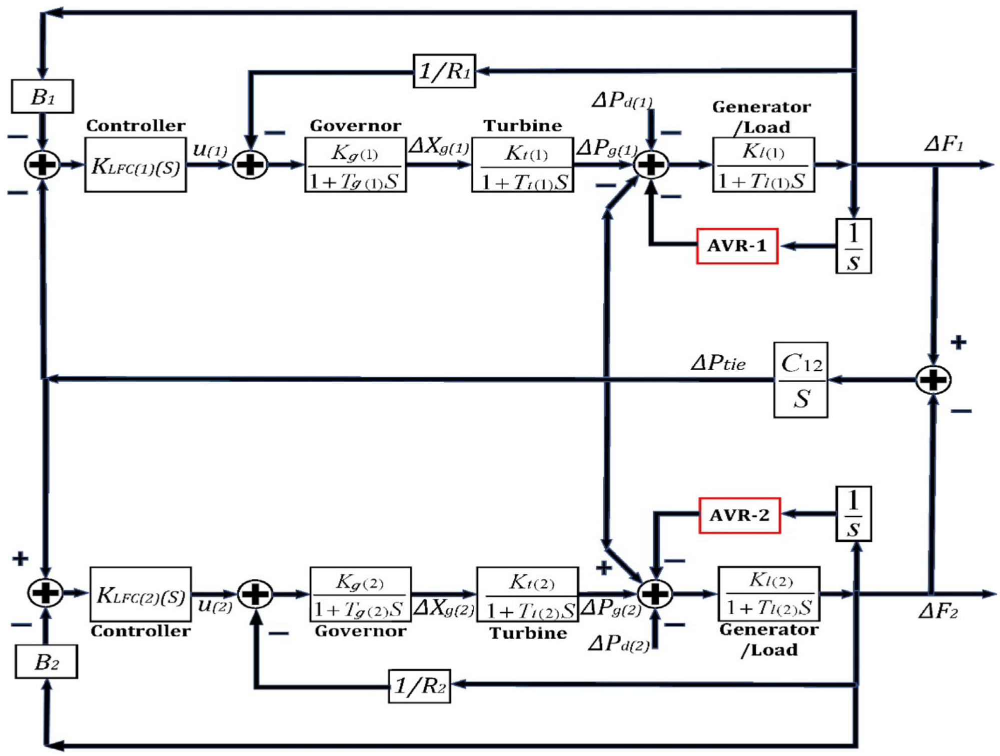

Fig. 1. Combined LFC-AVR model of Two-area system.

AVR loop is connected to the LFC loop for each area. Controlling the output voltages of the generating units is the responsibility of the AVR loop system, whereas the LFC loop system's focus is on regulating frequency variations brought on by active load disturbances (Gozde and Taplamacioglu, 2011; Gaing, 2004). The variations in the active load that occur in one region are not just reflected in the frequency variations that occur in that region; rather, they also serve as a source of disturbance for the other regions that are linked. In addition, Fig. 1 clarifies how the two areas are connected using a tie-line, which is also the channel via which power is transferred from one area to another. The total coupling of the two-area power system may be thought of as a graphical system, with the synchronization coefficient C12 serving as a representation of the graph weights (Nahas et al., 2021). This synchronization-like system depicts a consensus process for each region, where the states are the frequency-deviation values that reflect the various parts of the power system. The entire synchronization speed is determined by the synchronization coefficient. In the sections that follow, each part of the dynamical structure of the combined AVR-LFC scheme is explained in more detail.

2.1.1. Automatic voltage regulation

The AVR system aim is to minimize reactive power losses caused by voltage mismatches between targeted voltages and the exciter terminal voltage V_e. Variations in a generator's reactive power load cause changes in the terminal voltage V_g. As shown in Fig. 2, this voltage is detected using a single-phase potential transformer (i.e., voltage V_s) and then compared to a desired reference voltage V_{Ref}. The error signal is amplified (i.e., voltage V_a) and used to control the exciter's field and hence the exciter's terminal voltage. This causes changes in the generator's field current and, as a result, changes in the induced emf (Nahas et al., 2021). Table 1 shows the detailed mathematical modeling of the AVR unit.

2.1.2. Load frequency control

As depicted in Fig. 1, an LFC-based power system includes a rotating mass, governor, turbine, and load demands. The LFC structure's major objective is to split dynamic load changes among the various generators, maintain uniform frequency operating values, and govern tie-line exchange schedules (Hasanien and El-Fergany, 2019). The variations in frequency ΔF for each location reflect changes in the generator's rotor angle $\Delta\delta$. The frequency shift is detected, and the error signal is amplified and regulated before being utilized to create a real-power correction ΔP_g (Saadat, 2011). The prime mover is commanded to produce a torque variation via the real-power correction. Three basic differential equations are used to describe the LFC dynamical scheme, demonstrating the relationship between the Governor (a physical actuation system), Turbine, and Generator/Load units (Saadat, 2011; Hasanien and El-Fergany, 2019). These equations can be mathematically modeled for a single-area power system as shown in Table 2. The governor's dynamical behavior ΔX_g demonstrates that the signal u activates the governor's valve openings when it is accompanied by a negative feedback loop with a gain of $1/R$, as seen in Fig. 1. The governor actuation function is based on the LFC control gains and the speed regulation term R, with the linked load frequency deviations serving as inputs. As a result, the frequency fluctuation ΔF caused by load variations within each power system area is regulated by the LFC control signal u, which is the controller's output signal.

2.1.3. Combined AVR-LFC power system

The AVR and LFC systems' modest dynamical coupling allowed for independent control schemes for the voltage and frequency variables in each area. But, the AVR system's activities cause a terminal voltage change, which has a considerable impact on real power generation (Rajbongshi and Saikia, 2017b). As a result, the automatic voltage regulator has an immediate and significant effect on the load frequency control loop. Fig. 2 depicts the AVR loop with coupling coefficients. This coupling scheme describes

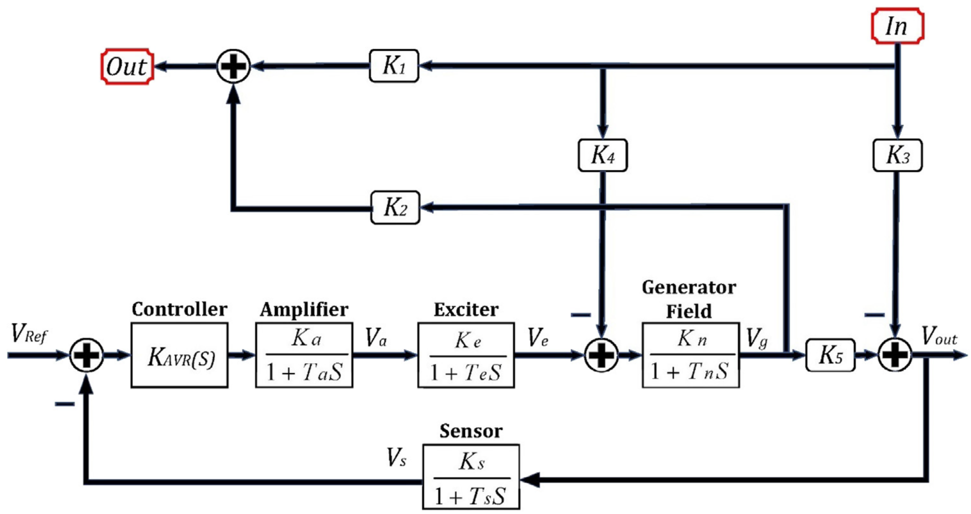

Fig. 2. AVR with coupling coefficients.

Table 1
AVR system modeling and setting.

Model	Transfer function	Parameters	Nominal values	Parameter description
Amplifier	$\frac{K_a}{1+T_a S}$	K_a, T_a	10, 0.1	Gains and time constants of amplifier, exciter, generator and sensor.
Exciter	$\frac{K_e}{1+T_e S}$	K_e, T_e	1, 0.4	
Generator	$\frac{K_n}{1+T_n S}$	K_n, T_n	1, 1	
Sensor	$\frac{K_s}{1+T_s S}$	K_s, T_s	1, 0.01	

Table 2
LFC system modeling and setting.

Model	Transfer function	Parameters	Nominal values	Parameter description
Governor	$\frac{K_g}{1+T_g S}$	K_g, T_g	1, 0.08	Gains and time constants of governor, turbine and generator/load
Turbine	$\frac{K_t}{1+T_t S}$	K_t, T_t	1, 0.3	
Generator/Load	$\frac{K_l}{1+T_l S}$	K_l, T_l	120, 20	
–	–	B_1, B_2	1, 1	Frequency bias coefficients
–	–	R_1, R_2	2.4, 2.4	Governor speed regulation parameters

the relationship between minor changes in stator emf on real electric power (K_2), small changes in rotor angle on terminal voltage (K_3), the effect of tiny rotor angle changes on stator emf (K_4), and the effect of small stator emf changes on rotor angle (K_5) (Nahas et al., 2021). The values of the coupling coefficients are taken as: $K_1 = 1.5$, $K_2 = 0.3$, $K_3 = 0.1$, $K_4 = 1.4$, and $K_5 = 0.5$. The nominal value of the synchronization coefficient (C_{12}) between the two areas is given as: $C_{12} = 0.545$.

2.2. The configuration of the hybrid power system

In this work, the problem of the combined LFC-AVR in relevance to electrical power grids is discussed by researching dual-area interconnected hybrid power systems. The investigated power grid consists of two interconnected areas in which area.1 has a thermal unit, hydropower unit, gas unit, and PV unit, and area.2 has the same conventional units as the area.1, but instead of the PV unit, a wind unit is inserted into area.2, as presented in Fig. 3. In this system, the conventional units have 2000 MW of rated power for each area, of which the thermal power unit provides 1000 MW, accounting for the majority of the electrical power share, afterwards we have the hydropower unit, which provides 500 MW, and the gas turbine, which supplies 240 MW to the whole output. And, the renewable units have 120 MW of rated power, of which the PV power unit supplies 50 MW, and the wind power unit provides 70 MW with a nominal load of 1740 MW for each area. Refs. Morsali et al. (2018) and SinghParmar et al. (2012) provide more information about the system under study and its parameters. Additionally, the system nonlinearities are taken into account, as are the power system's physical restrictions, such as the GRC and GDB of the thermal power plants, in which the GRC (generation rate constraint) of the hydropower station is 270% p.u/min = (0.045 p.u MW/s) and 360% p.u/min = (0.06 p.u MW/s), respectively for both rising and decreasing rates and the GRC for the thermal unit is set at 10% p.u/min (0.0017 p.u MW/s) for rising and decreasing rates. The transfer functions included in the considered power system have been listed in Table 3, and their configurations are made clear in Table 4.

2.2.1. The setup of PV generation model

Fig. 4 depicts how the Photovoltaic (PV) model may be constructed using the professional software MATLAB/SIMULINK (R2020a). The output power generated by the model is equivalent to the generated output power provided by an actual PV plant. In addition, about 50 MW of the PV model's output power permeates the first area of the examined power system. Here, Utilizing

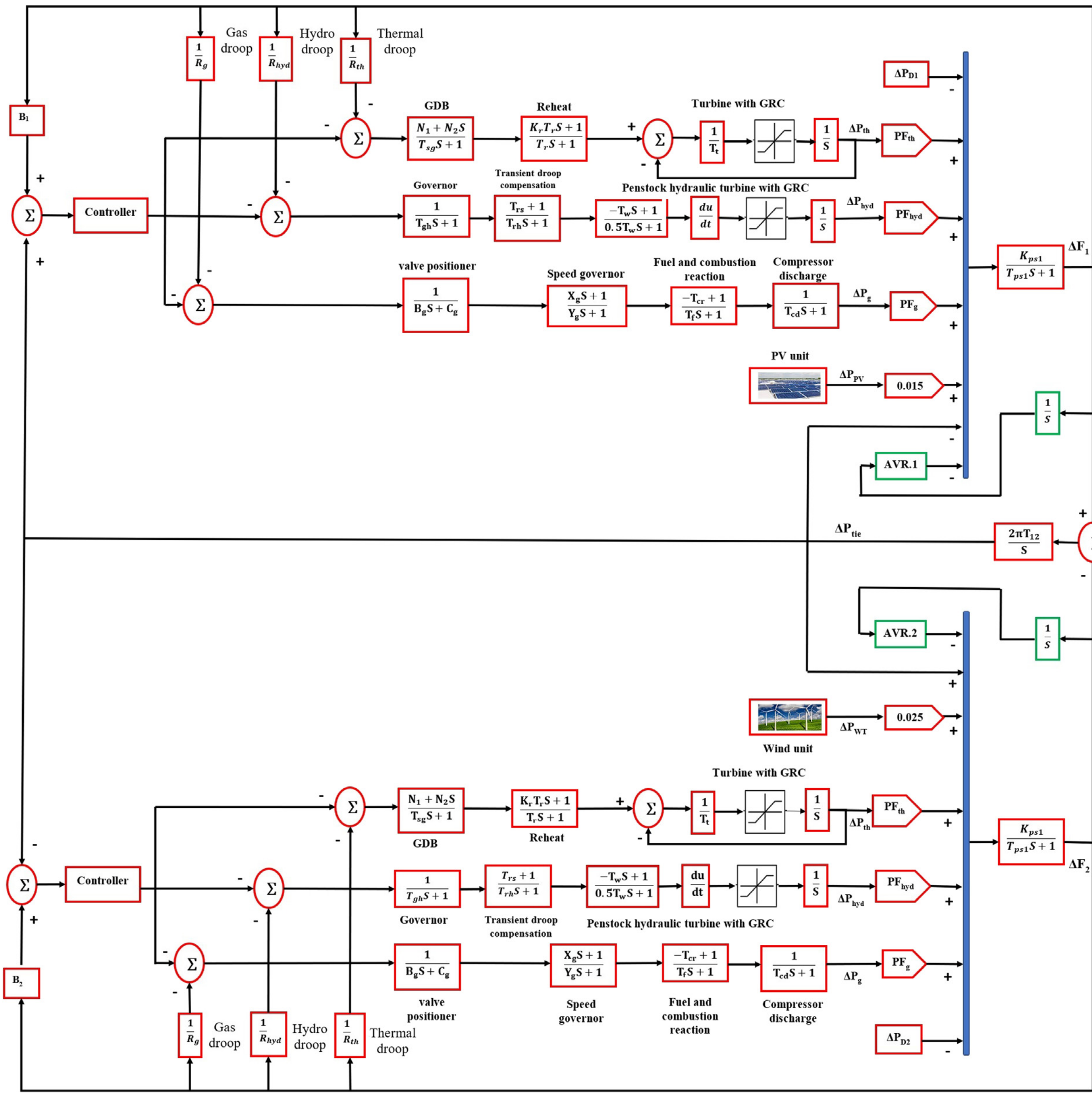

Fig. 3. The investigated dynamic model consisting of a two-area hybrid power system with various sources.

the white-noise block found inside the R2020a version of the MATLAB program allows for the production of random output fluctuations, which are then multiplied by the typical output power of an actual PV plant. The power generated by the proposed PV model may be calculated using Eq. (1) (Khamari et al., 2020). Fig. 5 presents the random power output generated by the PV model.

$$\Delta P_{Solar} = 0.6 \cdot \sqrt{P_{Solar}} \quad (1)$$

2.2.2. The setup of wind generation model

In order to apply the simplified model of wind generation power in order to share its power in the second area of the power system that is being studied, the expert software MATLAB/SIMULINK program (R2020a) is being utilized. The power created by the following wind power model behaves exactly the same as the electricity generated by actual wind farms, hence the model is quite accurate. This is accomplished with the use of a white-noise block, which is employed for making an arbitrary speed form and is then multiplied by the speed of the wind, as seen in Fig. 6 (Elkasem et al., 2021). The irregular output power of 93 wind units is depicted in Fig. 7, where each wind unit produces 0.75 MW of power. The value of the power generated by the wind farm that was investigated is around 70 MW. Following is a set of equations that may be used to describe the output power that was captured from the wind model (Elkasem et al., 2021):

$$P_W = 1/2 \rho A_T V_W^3 \, C_P(\lambda, \beta) \quad (2)$$

$$C_P(\lambda, \beta) = C_1 \cdot \left(\frac{C_2}{\lambda_I} - C_3\beta - C_4\beta^2 - C_5 \right) \cdot e^{\frac{C_6}{\lambda_I}} + C_7\lambda_T \quad (3)$$

$$\lambda_T = \lambda_T^{OP} = \frac{\omega_T \cdot r_T}{V_W} \quad (4)$$

$$\frac{1}{\lambda_I} = \frac{1}{\lambda_T + 0.08\beta} - \frac{0.035}{\beta^3 + 1} \quad (5)$$

In Eq. (2), P_W denotes the wind turbine output power, ρ denotes the air density in kg/m^3, A_T denotes the swept area by the rotor in m^2, V_W denotes the wind's nominal speed in m/s, and C_P denotes the rotor's blade parameter. In Eq. (3), C_1 to C_7 denote the parameters of the turbine, β denotes the pitch angle of the blade,

Table 3
Transfer functions of the system model.

Power planet	Model	Transfer function
Thermal	GDB	$\frac{N_1+N_2S}{T_{sg}S+1}$
	Reheat	$\frac{k_rT_rS+1}{T_rS+1}$
Hydraulic	Governor	$\frac{1}{T_{gh}S+1}$
	Transient droop compensation	$\frac{T_{rs}S+1}{T_{rh}S+1}$
	Penstock hydraulic turbine	$\frac{-T_wS+1}{0.5T_wS+1}$
Gas	Valve positioner	$\frac{1}{B_gS+C_g}$
	Speed governor	$\frac{X_gS+1}{Y_gS+1}$
	Fuel combustion reaction	$\frac{-T_{cr}S+1}{T_fS+1}$
	Compressor discharge	$\frac{1}{T_{cd}S+1}$
AVR	Amplifier	$\frac{K_a}{1+T_aS}$
	Exciter	$\frac{K_e}{1+T_eS}$
	Generator	$\frac{K_n}{1+T_nS}$
	Sensor	$\frac{K_s}{1+T_sS}$
Others	Power system 1	$\frac{K_{ps1}}{T_{ps1}S+1}$
	Power system 2	$\frac{K_{ps2}}{T_{ps2}S+1}$
	T-line	$\frac{2\pi T_{12}}{S}$

λ_T denotes the optimal tip speed ratio (TSR), and λ_I denotes the intermittent tip speed ratio. In Eq. (4), r_T denotes the radius of the rotor. The nominal wind generation coefficients are listed in Table 5.

3. Control strategy and problem definition

3.1. Gradient-based optimization algorithm

Ahmadianfar et al. (2020) proposed the GBO method, which is among the most recent metaheuristic optimization techniques. GBO's operation is made up of two concepts: gradient-based

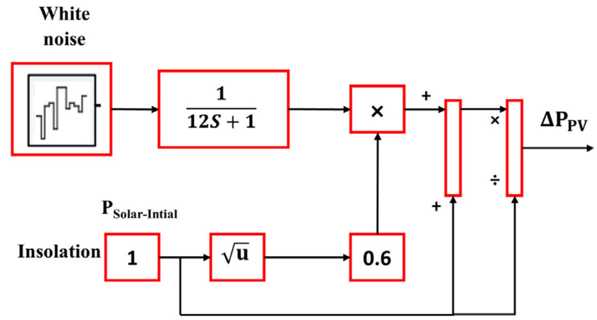

Fig. 4. The PV model.

Newton's phenomenon and two trajectories for diversification and intensified search. The Gradient Search Rule (GSR) trajectory facilitates exploration and accelerates convergence to get the optimum fitness in the search space. The Local Escaping Operator (LEO) trajectory, on the other hand, serves the primary purpose of allowing the GBO to flee from the local solution. A graphic representation of the GBO algorithm's operation is presented in Fig. 8. In order to facilitate comprehension, the GBO algorithm's working mechanism has been broken down into the steps listed below.

3.1.1. Initialization

Individually, the GBO creates a main population from a uniform arbitrary distribution. In a population with N trajectories, each agent is given the term "trajectory", and the population is free to explore a domain with D dimensions. The following mathematical statement represents the initialization procedure.

$$X_n = X_{min} + rand\,(0,\,1)\cdot(X_{max} - X_{min}) \tag{6}$$

where X_{min} and X_{max} are the decision variable X boundaries, and $rand\,(0,\,1)$ represents an arbitrary value within the range [0 1].

Table 4
The power system settings.

Settings	Value	Settings description
N_1, N_2	0.8, $-0.2/\pi$	The GDB transfer function model's Fourier coefficients
T_{sg}	0.06 s	Steam turbine governor time constant
T_t	0.3 s	Steam turbine time constant
T_r	10.2 s	Steam turbine reheat time constant
K_r	0.3	Reheat constant of the steam turbine
T_w	1.1 s	Starting time of water in the hydro turbine
T_{rs}	4.9 s	Hydro turbine speed governor reset time
T_{rh}	28.749 s	Time constant of the transient droop
T_{gh}	0.2 s	Hydro turbine governor time constant
B_g	0.049 s	Time constant of the valve positioner
Y_g	1.1 s	Lag time constant of gas turbine governor
T_{cr}	0.01 s	Time delay of the gas turbine combustion reaction
T_f	0.239 s	Gas turbine fuel time constant
X_g	0.6 s	Lead time constant of gas turbine governor
T_{cd}	0.2 s	Time constant of the compressor discharge volume
C_g	1	Gas turbine valve positioner
K_a, K_e, K_n, K_s	10, 1, 1, 1	AVR system amplifier, exciter, generator, and sensor gains
T_a, T_e, T_n, T_s	0.1, 0.4, 1, 0.01	AVR system amplifier, exciter, generator, and sensor time constants
T_{ps1}, T_{ps2}	11.49, 11.49 s	Power system time constants
K_{ps1}, K_{ps2}	68.965, 68.965	Power system gains
T_{12}	0.0433 MW	Synchronizing coefficient
B_1, B_2	0.431, 0.431 MW/Hz	Frequency bias coefficients
PF_{PV}, PF_{WT}	0.015, 0.025	PV and wind generation units' participation factors
R_{hyd}, R_g, R_{Th}	2.4, 2.4, 2.4 Hz/MW	Governor speed regulation parameters of thermal, hydro, and gas units
PF_{hyd}, PF_g, PF_{Th}	0.287, 0.138, 0.575	Participation factors of hydro, gas, and thermal units
GRC with Hydro	–	(0.045 p.u MW/s) and (0.06 p.u MW/s. For both rising and decreasing rates), respectively
GRC with Thermal	–	The GRC (generation rate constraint) for the thermal unit is set (0.0017 p.u MW/s) For rising and decreasing rates

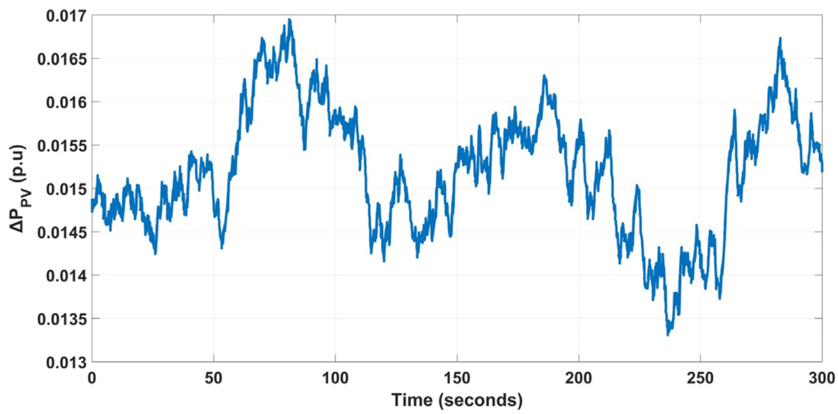

Fig. 5. PV power fluctuations.

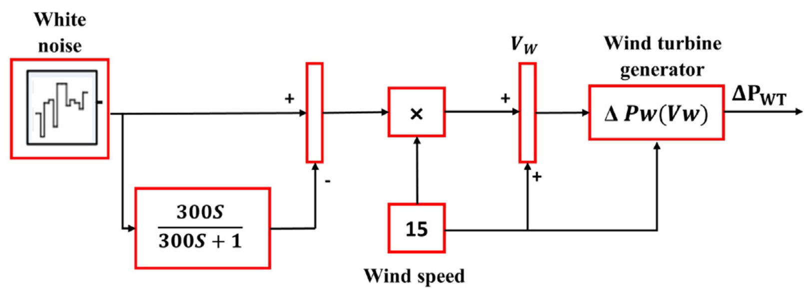

Fig. 6. The wind system model.

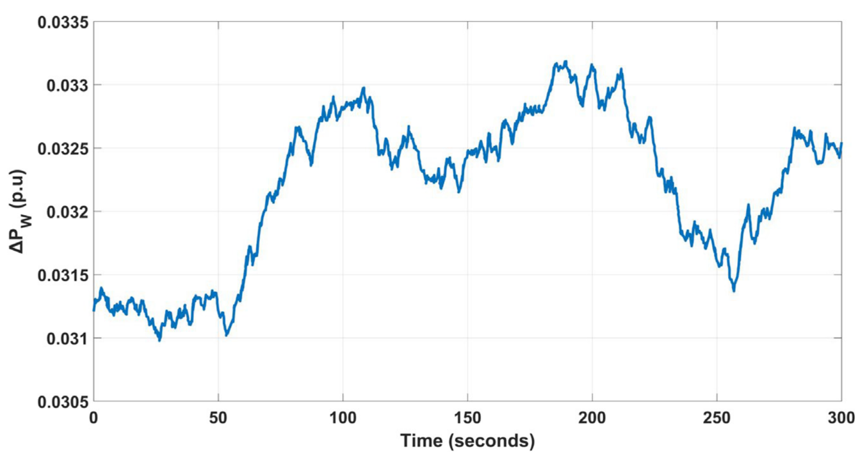

Fig. 7. Variation of wind power.

Table 5
The wind power plant coefficients.

Parameter	Value	Parameter	Value
P_W	750 kW	C_2	116
V_W	15 m/s	C_3	0.4
r_T	22.9 m	C_4	0
ρ	1.225 kg/m^3	C_5	5
A_T	1684 m^2	C_6	21
λ_T	22.5 r.p.m	C_7	0.1405
C_1	−0.6175		

3.1.2. Gradient search rule (GSR)

During the optimization process, the GSR in the algorithm is in charge of delivering unpredictable behavior that boosts the algorithm's diversion power. Based on the GSR, direction of movement (DM), and beginning location of the search agent, the location of the trajectory (x_n^m) may be computed using Eq. (7).

$$X1_n^m = x_n^m - GSR + DM \tag{7}$$

where,

$$GSR = randn \cdot \rho_1 \cdot \frac{2\Delta x \cdot x_n^m}{(x_{worst} - x_{best} + \varepsilon)} \tag{8}$$

$$DM = rand \cdot \rho_2 \cdot (x_{best} - x_n^m) \tag{9}$$

$$\rho_1 = 2 \cdot rand \cdot \alpha - \alpha \tag{10}$$

$$\alpha = \left| \beta \cdot sin\left(\frac{3\pi}{2} + sin\left(\beta \cdot \frac{3\pi}{2}\right)\right) \right| \tag{11}$$

$$\beta = \beta_{min} + (\beta_{max} - \beta_{min}) \cdot \left(1 - \left(\frac{m}{M}\right)^3\right)^2 \tag{12}$$

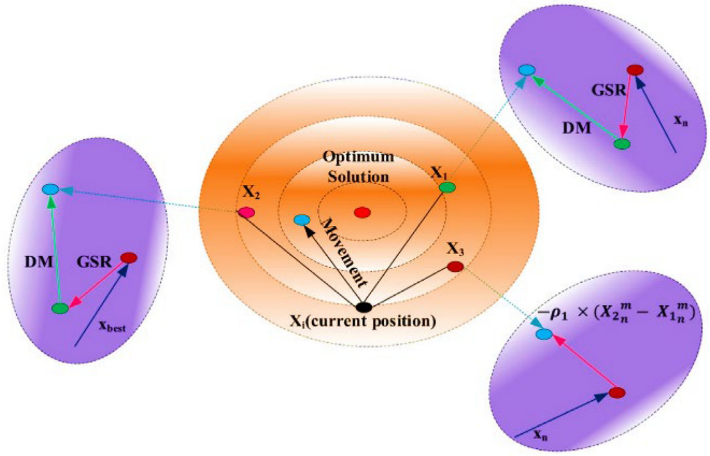

Fig. 8. The GBO technique scheme.

where m denotes the present iteration number, M represents the maximum number of iterations, β_{min} is 0.2, β_{max} is 1.2, and ε denotes a number between [0, 0.1]. ρ_2 may be computed as follows:

$$\rho_2 = 2 \cdot rand \cdot \alpha - \alpha \tag{13}$$

$$\Delta x = rand(1:N) \cdot |step| \tag{14}$$

$$step = \frac{\left(x_{best} - x_{r1}^m\right) + \delta}{2} \tag{15}$$

$$\delta = 2 \cdot \text{rand} \cdot \left(\left|\frac{x_{r1}^m + x_{r2}^m + x_{r3}^m + x_{r4}^m}{4} - x_n^m\right|\right) \tag{16}$$

*opensr*2, *r*3, and *r*4 ($r1 \neq r2 \neq r3 \neq r4 \neq n$) are numbers selected at random from [1 *N*], and $rand(1:N)$ is an N-dimensional arbitrary number. The *step* in Eq. (15) denotes the step size that is described by x_{best} and x_{r1}^m. By swapping the site of the best trajectory (x_{best}) with the current trajectory (x_n^m) found in Eq. (6), the new trajectory ($X2_n^m$) can be described as:

$$X2_n^m = x_{best} - randn \cdot \rho_1 \cdot \frac{2\Delta x \cdot x_n^m}{\left(yp_n^m - yq_n^m + \varepsilon\right)} + rand \cdot \rho_2 \cdot \left(x_{r1}^m - x_{r2}^m\right) \tag{17}$$

where,

$$yp_n = rand \cdot \left(\frac{[z_{n+1} + x_n]}{2} + rand \cdot \Delta x\right) \tag{18}$$

$$yq_n = rand \cdot \left(\frac{[z_{n+1} + x_n]}{2} - rand \cdot \Delta x\right) \tag{19}$$

the new solution at the next iteration (x_n^{m+1}), established on the locations $X1_n^m$, $X2_n^m$, and the current location (X_n^m), can be described as:

$$x_n^{m+1} = r_a \cdot \left(r_b \cdot X1_n^m + (1 - r_b) \cdot X2_n^m\right) + (1 - r_a) \cdot X3_n^m \tag{20}$$

$$X3_n^m = X_n^m - \rho_1 \cdot \left(X2_n^m - X1_n^m\right) \tag{21}$$

3.1.3. Local escaping operator (LEO)

Incorporating the LEO into GBO improves the algorithm's ability to resolve difficult optimization issues. Helps the algorithm break out of the "local optimality" trap. The LEO employs a number of solutions to arrive at the best solution (X_{LEO}^m), including the best location (x_{best}), the locations $X1_n^m$ and $X2_n^m$, two arbitrary locations x_{r1}^m and x_{r2}^m, and a contemporaneous arbitrarily produced location (x_k^m). The following methodology is used to construct the answer X_{LEO}^m.

$$\begin{aligned}
&\textit{if rand} < pr \\
&\qquad\qquad\qquad\qquad \textit{if rand} < 0.5 \\
&X_{LEO}^m = X_n^{m+1} + f_1 \cdot \left(u_1 \cdot x_{best} - u_2 \cdot x_k^m\right) \\
&\quad + f_2 \cdot \rho_1 \cdot \left(u_3 \cdot \left(X2_n^m - X1_n^m\right) + u_2 \cdot \left(x_{r1}^m - x_{r2}^m\right)\right)/2 \\
&X_n^{m+1} = X_{LEO}^m \\
&else \\
&X_{LEO}^m = x_{best} + f_1 \cdot \left(u_1 \cdot x_{best} - u_2 \cdot x_k^m\right) \\
&\quad + f_2 \cdot \rho_1 \cdot \left(u_3 \cdot \left(X2_n^m - X1_n^m\right) + u_2 \cdot \left(x_{r1}^m - x_{r2}^m\right)\right)/2 \\
&X_n^{m+1} = X_{LEO}^m \\
&\qquad\qquad\qquad\qquad End \\
&End
\end{aligned} \tag{22}$$

where f_1 is an even arbitrary number, f_2 is an arbitrary number in a normal distribution with a zero mean and a unity standard deviation, *pr* is the probability, and u_1, u_2, and u_3 are three arbitrary values, which are given as:

$$u_1 = \begin{cases} 2 \cdot rand\,if\ \ \mu_1 < 0.5 \\ 1 \quad otherwise \end{cases} \tag{23}$$

$$u_2 = \begin{cases} rand\,if\ \ \mu_1 < 0.5 \\ 1 \ \ otherwise \end{cases} \tag{24}$$

$$u_3 = \begin{cases} rand\,if\ \ \mu_1 < 0.5 \\ 1 \ \ otherwise \end{cases} \tag{25}$$

where *rand* denotes an arbitrary value within the domain [0 1], and μ_1 denotes a value within the domain [0 1]. We can rewrite the above-mentioned equations as:

$$u_1 = L_1 \cdot 2 \cdot rand + (1 - L_1) \tag{26}$$

$$u_2 = L_1 \cdot rand + (1 - L_1) \tag{27}$$

$$u_3 = L_1 \cdot rand + (1 - L_1) \tag{28}$$

where L_1 represents a binary parameter, whose value is 0 or 1. If the value of the parameter μ_1 gets smaller than 0.5, the value of L_1 becomes 1, otherwise, it becomes 0. To describe the solution x_k^m in Eq. (6), The strategy may be expressed mathematically as follows:

$$x_k^m = \begin{cases} x_{rand} & if\ \ \mu_2 < 0.5 \\ x_p^m & otherwise \end{cases} \tag{29}$$

$$x_{rand} = X_{min} + rand\,(0, 1) \cdot (X_{max} - X_{min}) \tag{30}$$

Table 6
The best objective functions obtained by the four algorithms.

Test functions		The best objective function obtained			
		GTO	ChOA	WHO	GBO
$f_1(x)$	$x_1^2 + 10^6 \sum_{i=2}^{D} x_i^2$	6.6×10^{-29}	1.8×10^{-5}	3.8×10^{-50}	1.4×10^{-121}
$f_2(x)$	$\sum_{i=1}^{D} \lvert x_i \rvert^{i+1}$	8×10^{-103}	2.2×10^{-17}	1.4×10^{-107}	8.2×10^{-188}
$f_3(x)$	$\sum_{i=1}^{D} x_i^2 + \left(\sum_{i=1}^{D} 0.5x_i\right)^2 + \left(\sum_{i=1}^{D} 0.5x_i\right)^4$	2.8×10^{-32}	3.4×10^{-5}	1.8×10^{-50}	2.4×10^{-128}
$f_4(x)$	$\sum_{i=1}^{D-1} \left[100\left(x_{i+1} - x_i^2\right)^2 + (x_i - 1)^2\right]$	27.13	28.94	25.64	20.14
$f_5(x)$	$10^6 x_1^2 + \sum_{i=2}^{D} x_i^2$	6.3×10^{-33}	4.6×10^{-13}	6.9×10^{-49}	1.9×10^{-126}
$f_6(x)$	$\sum_{i=1}^{D} \left(10^6\right)^{\frac{i-1}{D-1}} x_i^2$	1.6×10^{-32}	2.3×10^{-7}	4.6×10^{-55}	1.4×10^{-130}

Step 1. Initialization
Assign values for parameters pr, ε, and M
Generate an initial population $X_0 = [x_{0,1}, x_{0,2}, ..., x_{0,D}]$
Evaluate the objective function value $f(X_0),\ n = 1, ..., N$
Specify the best and worst solutions x_{best}^m and x_{worst}^m
Step 2. Main loop
While ($m<M$)
for $n = 1 : N$
for $i = 1 : D$
Select randomly $r1 \neq r2 \neq r3 \neq r4 \neq n$ in the range of $[1, N]$
Calculate the position $x_{n,i}^{m+1}$ using Eq. 20
end for
Local escaping operator
if $rand < pr$
Calculate the position x_{LEO}^m using Eq. 22
$X_n^{m+1} = x_{LEO}^m$
end
Update the positions x_{best}^m and x_{worst}^m
end for
m=m+1
end
Step 3. return x_{best}^m

Fig. 9. The pseudo-code that represents the GBO algorithm (Ahmadianfar et al., 2020).

where x_{rand} denotes a new solution, x_p^m is a randomly chosen solution of the population ($p \in [1, 2, 3, \ldots\ldots, N]$), and μ_2 is an arbitrary number within the domain [0 1]. Eq. (29) can be re-written in a simplified expression as:

$$x_k^m = L_2 \cdot x_p^m + (1 - L_2) \cdot x_{rand} \tag{31}$$

where L_2 represents a binary parameter, whose value is 0 or 1. If the value of the parameter μ_2 gets smaller than 0.5, the value of L_2 becomes 1, elsewise, it becomes 0. Fig. 9 (Ahmadianfar et al., 2020) provides an overview of the pseudo-code for the GBO algorithm. The flowchart of the approach that was employed to achieve the optimum gains of the suggested FPIDD^2 regulator in this work can be seen in Fig. 10.

Finally, six commonly used benchmark functions from previous research (Khishe and Mosavi, 2020; Abdollahzadeh et al., 2021; Ahmadianfar et al., 2020) are used to comprehensively evaluate the performance of the GBO algorithm. The effectiveness of GBO is evaluated by comparing it with three other metatheuristic algorithms (GTO, ChOA and WHO). 30 iterations of each optimization procedure are performed for each test function. A maximum number of 500 iterations was allowed, and the population size was set to 50. Table 6 summarizes the best objective functions obtained by the four algorithms. Fig. 11 shows GBO convergence curves and other algorithms that have been realized in the tested benchmark functions. The results highlight the advantage of GBO over competing algorithms.

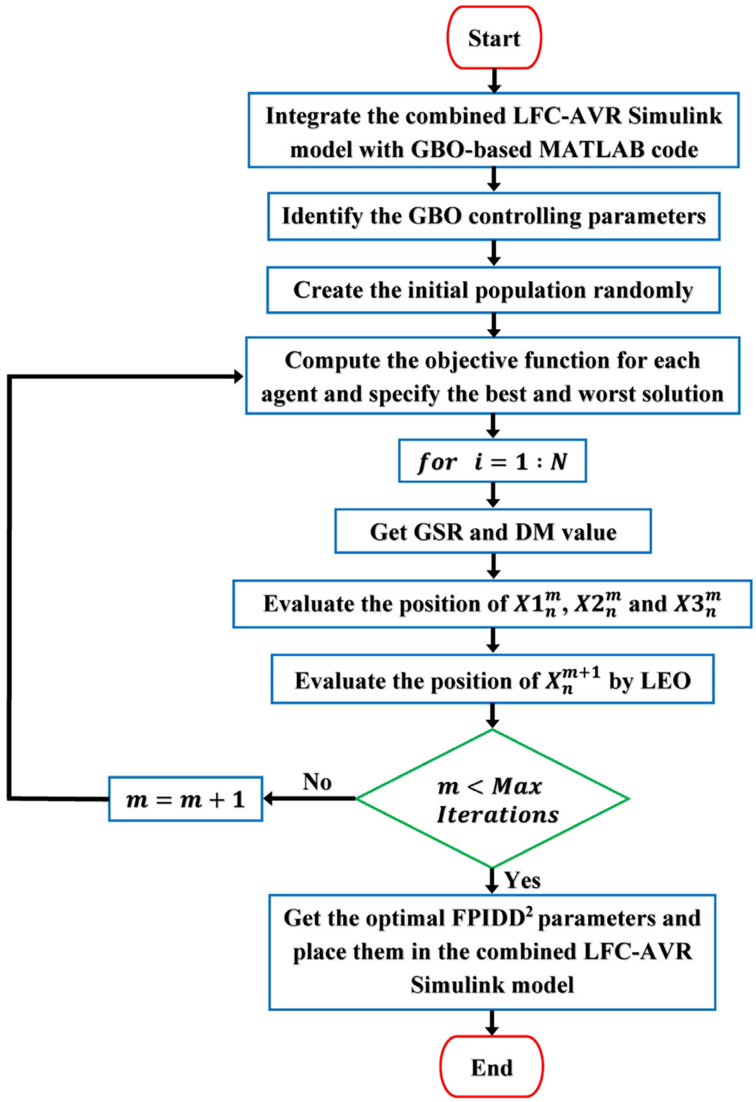

Fig. 10. The flowchart of the GBO technique adjusting FPIDD^2 settings.

3.2. Controller structure and suggested solution methodology

The current section discusses the design of the intelligent fuzzy PIDD^2 controller to handle the LFC problem, given that traditional controllers have certain flaws in coping with the uncertainties of the system derived from prior research. The suggested controller mingles the benefits of Fuzzy logic and PIDD^2 controllers, which ultimately allows for superior load frequency regulation. The PIDD^2 controller setup is exactly the same as that of the PID controller, with the addition of a second derivative action to the standard PID components. Fig. 12.a denotes the structure of PIDD^2 regulator. Eq. (32) (Kalyan and Suresh, 2021) is a representation of the PIDD^2 controller's transfer function.

$$C_1(s) = K_P + \frac{K_I}{s} + K_{D1}\cdot s\left[\frac{N_1}{s+N_1}\right] + K_{D1}K_{D2}\cdot s^2\left[\frac{N_1N_2}{(s+N_1)(s+N_2)}\right] \tag{32}$$

where K_P, K_I, (K_{D1}, K_{D2}) and (N_1, N_2) represent the proportional gain, integral gain, derivative gains, and filter coefficients, respectively, of the PIDD^2 controller.

Additionally, a fuzzy logic controller, also known as an FLC, may be attached to the PIDD^2 regulator in order to enhance both its functionality and its effectiveness. However, the effectiveness of fuzzy logic regulators is highly dependent on the membership functions (MFs) and the convoluted development of a proper fuzzy rule base interface system. Fig. 12.b depicts the configuration of the FPIDD^2 controller used for the combined LFC and AVR investigation where the error input (E) and the change of error (CE) serve as inputs to the fuzzy controller. Scaling factors are represented by the gains K_1 and K_2. Following is a brief overview of the key procedures involved in deploying an FLC (Cam et al., 2017; Bhateshvar et al., 2017):

The first phase is called "fuzzification", and it involves the FLC converting E and CE into linguistic variables. For the sake of clarity, simplicity in real-time processing and the need for low-level memory (Tasnin and Saikia, 2018; Yakout et al., 2021), the inputs and outputs of the FLCs in this study are all triangular membership functions as shown in Fig. 13. Regarding the inputs and output, there are five linguistic variables employed, including LN, SN, Z, SP, and LP, denoting large negative, small negative, zero, small positive, and large positive. It is clear that the membership functions of both inputs and output are located in the interval [−40, 40]. The implementation of the rule base constitutes the second phase of the process. Table 7 displays the results of the FLC's application of fuzzy rules to the linguistic variables derived from the fuzzification process; the FIS utilized in this case is Mamdani (Yakout et al., 2021). It is up to the designer's skill level

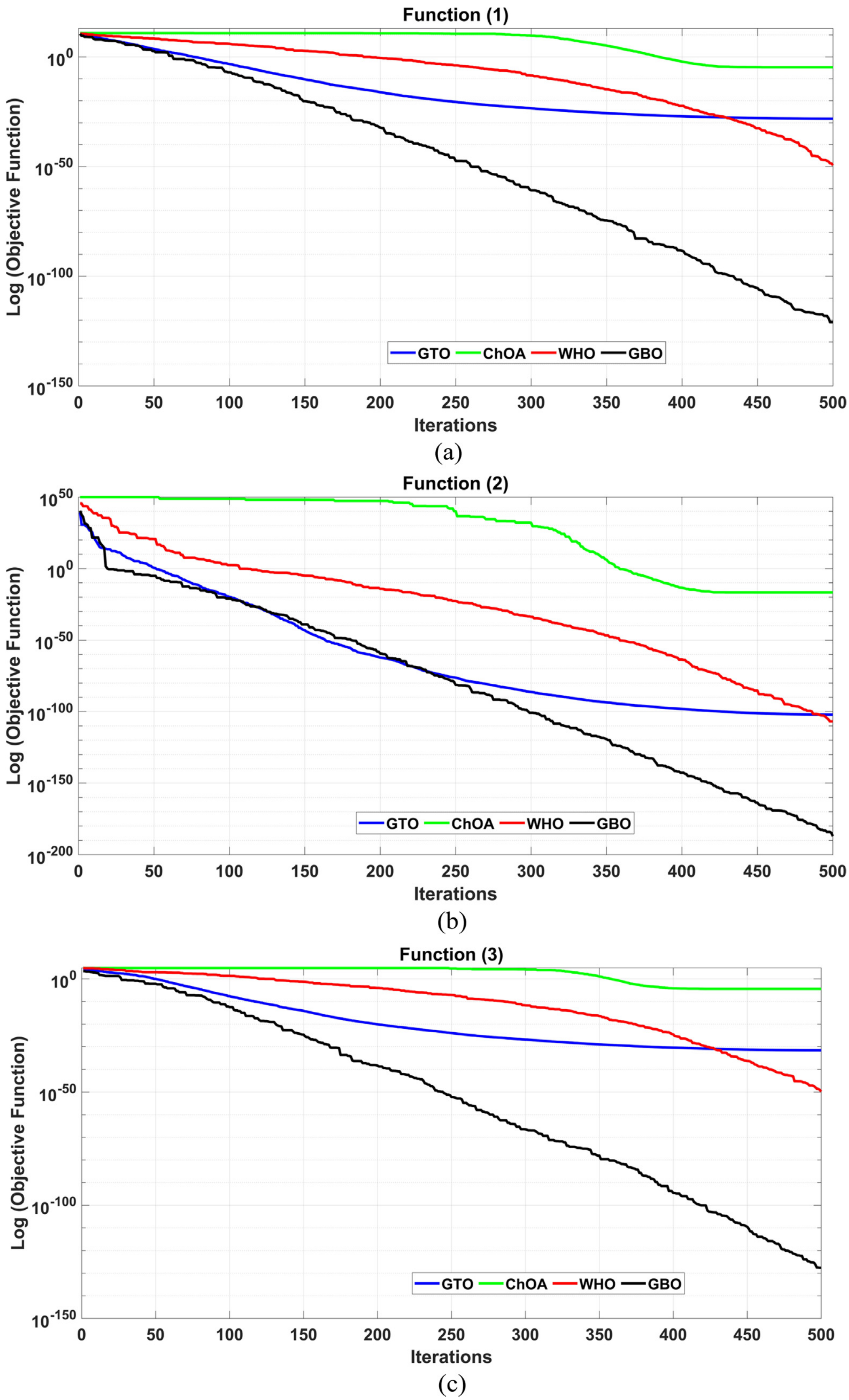

Fig. 11. The convergence curves of the four comparative algorithms achieved in some popular benchmark functions.

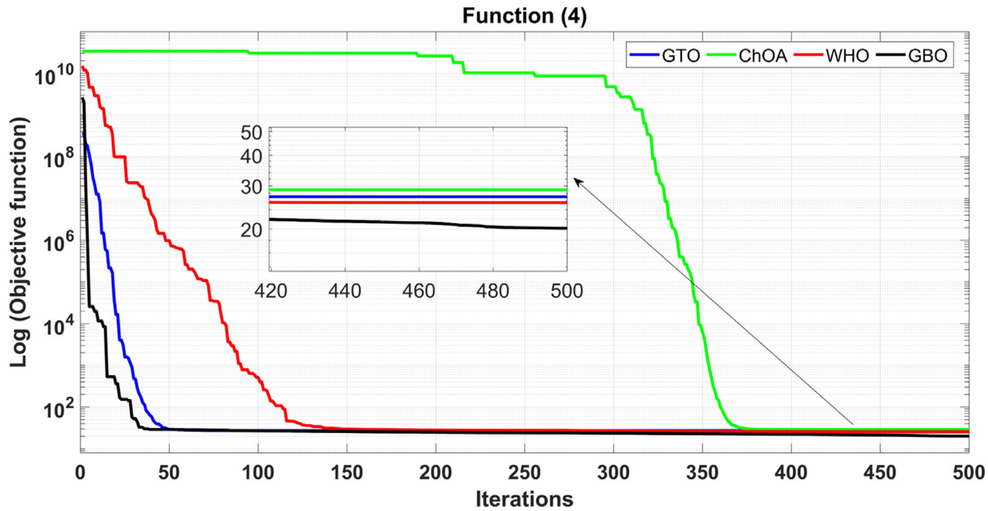

(d)

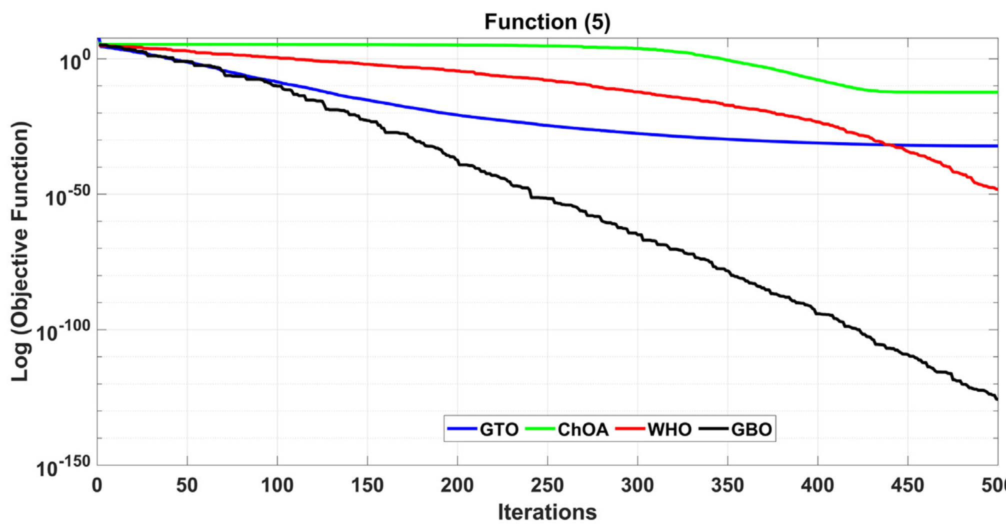

(e)

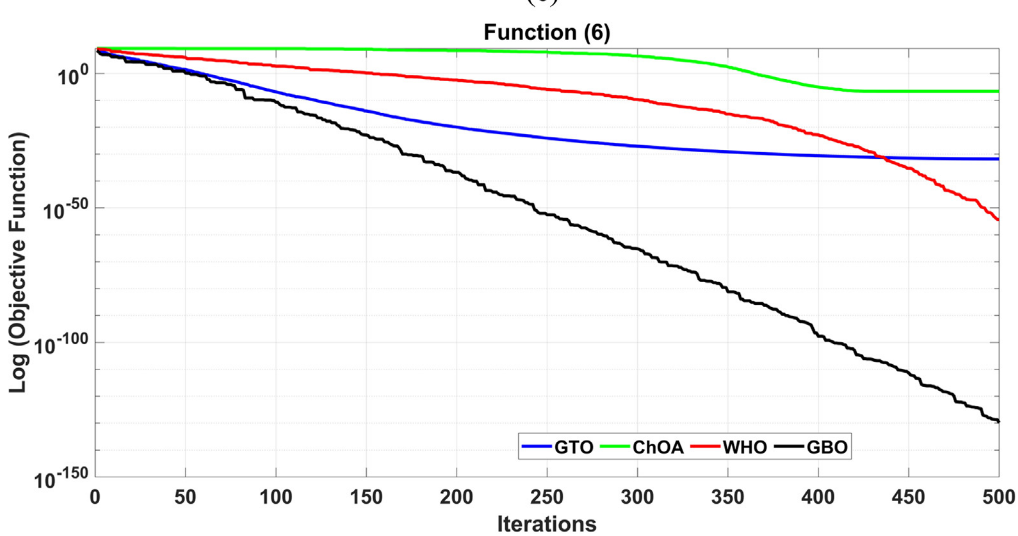

(f)

Fig. 11. (*continued*).

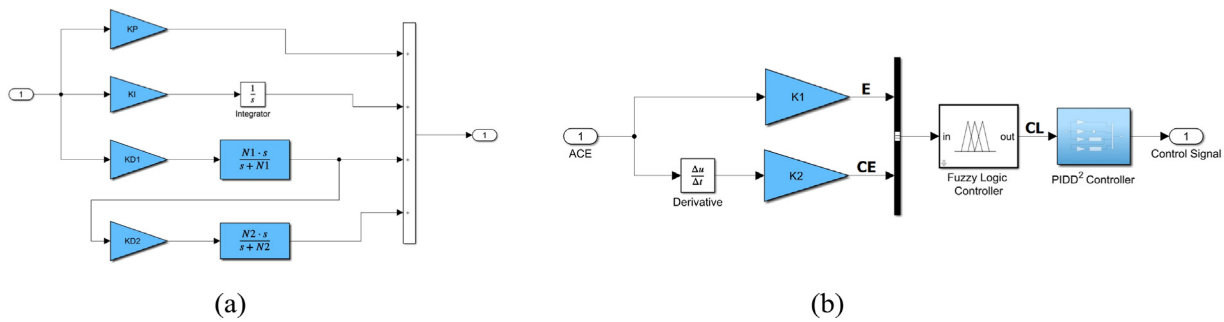

Fig. 12. (a) The structure of PIDD^2 controller, (b) The configuration of the FPIDD^2 controller.

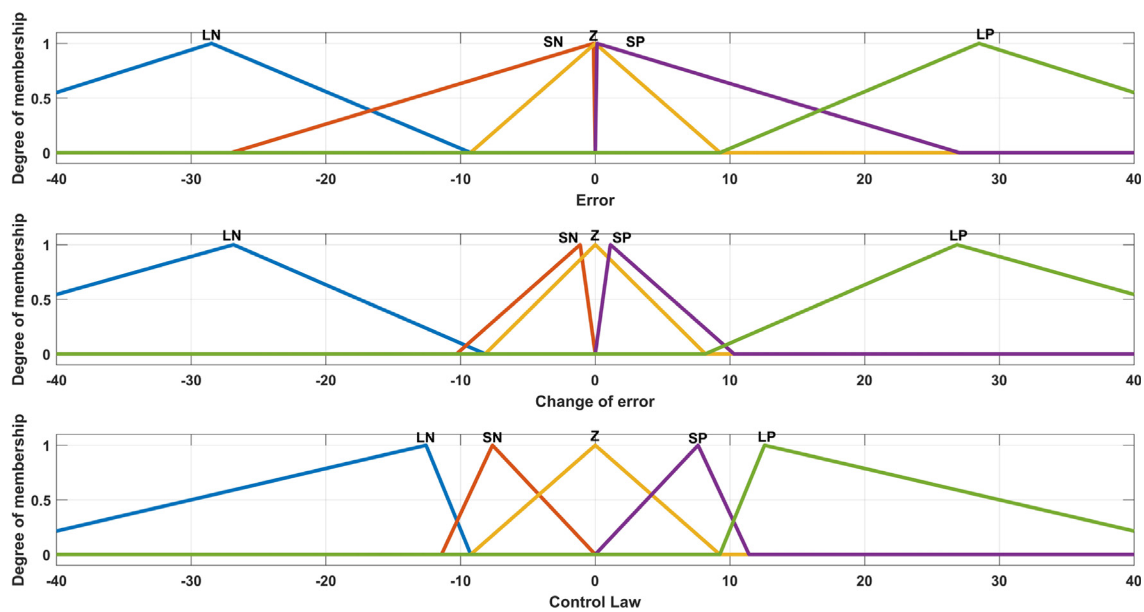

Fig. 13. Membership functions for the FLC.

to determine the scope and nature of the FLC's underlying rule set. Each system relies on its own set of rules to get the best possible outcome.

Reaching the final phase, which is called defuzzification. The defuzzification procedure takes in linguistic variables as inputs, and the output of the FIS system is itself a linguistic variable. additionally, the defuzzification procedure transforms these variables to crisp variables. In this work, the fuzzy output Control Law (CL) was calculated using the defuzzification procedure's center of gravity approach. The CL signal is passed to PIDD^2 controller. Fig. 14 depicts the control surface that represents the FLC's input–output correlation. It is a tough challenge to determine the optimal input and output values and shapes for FLC. The primary objective of the suggested controller is to lessen frequency deviation (ΔF_1, ΔF_2) and lower tie-line power deviations ($\Delta P_{tie-line}$), caused by system uncertainties, in the LFC loop, and improve the dynamic response of the voltage in both areas by lowering the voltage deviations (ΔV_1, ΔV_2). This may be accomplished by fine-tuning the FPIDD^2 controller's settings ($K_P, K_I, K_{D1}, K_{D2}, N_1, N_2, K_1, K_2$).

In this study, the integral time absolute error, often known as ITAE, was chosen to serve as the objective function for evaluating the controller's performance. According to Eq. (33) (Kalyan, 2021), ITAE is expected to be the method that is most successful in significantly lowering response overshoots and settling time in the combined LFC-AVR problem .

$$ITAE = \int_0^{T_{sim}} t \cdot (|\Delta F_1| + |\Delta F_2| + |\Delta P_{tie-line}| + |\Delta V_1| + |\Delta V_2|)\, dt \tag{33}$$

where T_{sim} represents simulation time. The parameters of the controller are regulated as follows:

$$\begin{cases} K_{P\,min} \le K_P \le K_{P\,max} \\ K_{I\,min} \le K_I \le K_{I\,max} \\ K_{D1\,min} \le K_{D1} \le K_{D1\,max} \\ K_{D2\,min} \le K_{D2} \le K_{D2\,max} \\ N_{1\,min} \le N_1 \le N_{1\,max} \\ N_{2\,min} \le N_2 \le N_{2\,max} \\ K_{1\,min} \le K_1 \le K_{1\,max} \\ K_{2\,min} \le K_2 \le K_{2\,max} \end{cases} \tag{34}$$

For all following Cases, the lower bounds are set [0, 0, 0, 0, 100, 100, 0, 0] while the higher bounds are set [4, 4, 4, 2, 500, 500,

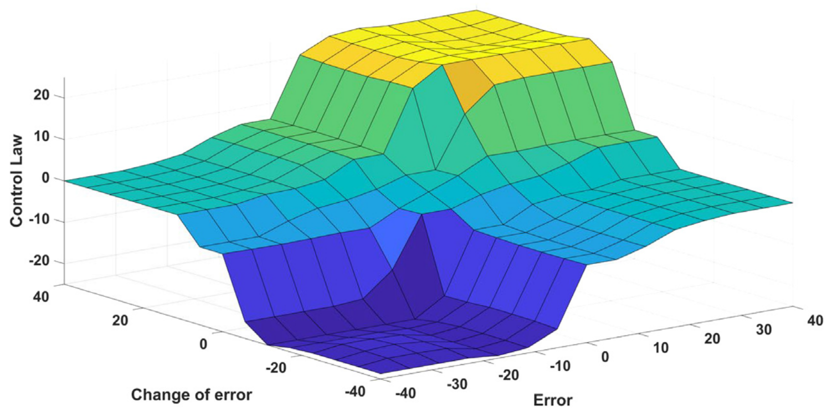

Fig. 14. Rule surface viewer of the FLC.

Table 7
The fuzzy Logic controller's rule base.

E	CE				
	LN	SN	Z	SP	LP
LN	LN	LN	SN	SN	Z
SN	LN	SN	SN	Z	SP
Z	SN	SN	Z	SP	SP
SP	SN	Z	SP	SP	LP
LP	Z	SP	SP	LP	LP

4, 4]. The frequency limits are assumed to be ±1 Hz, the tie-line power limits are taken as ±10%, and the voltage limits are assumed to be ±5% (Nahas et al., 2019). The simulation's results and observations will be presented in the next section under a wide variety of different operating circumstances.

4. Numerical simulation and analysis

In this part of the paper, the dynamic performance of the previously presented power systems (i.e., conventional and hybrid) is evaluated under various cases:

(1) Conventional power system studied cases

- Tuning the AVR system individually.
- Tuning the LFC system individually.
- Tuning of combined LFC-AVR system.

All the previous cases are studied under nominal and disturbed system parameters.

(2) Hybrid power system studied cases

- Applying multi-step load perturbations (MSLP) in area -1.
- Applying communication time delay (CTD) to the controller output.
- Applying random load perturbations (RLP) in area-1 as well as a time-varying desired output voltage.
- Varying the parameters of the system.

RESs penetration is taken into account in all hybrid power system studied cases.

In the conventional system that has been analyzed, the PID controller that has been tuned using MONLTA (Nahas et al., 2021) and the FPID controller that has been tuned using GBO are compared with the newly suggested FPIDD^2 regulator. The suggested FPIDD^2 regulator is evaluated in the context of the examined hybrid system and contrasted with a GBO-tuned ID-T controller and an FPID controller.

In the following subsections, each system's dynamic performance has been studied, and every case has been discussed in detail. The optimization processes with the GBO are evaluated with a maximum iteration of 50 and a number of search agents of 20.

4.1. The conventional system cases

Firstly, the superiority of the GBO algorithm is proved by comparing it with other recent algorithms such as ChOA (Khishe and Mosavi, 2020), WOA (Mirjalili and Lewis, 2016) and GTO (Abdollahzadeh et al., 2021). The comparison is carried out on the basis of fine-tuning the proposed controller parameters to enhance the voltage and frequency stability of the combined LFC-AVR two-area power system under normal case in which the nominal values for the parameters of the combined LFC-AVR are considered in area-1, while a disturbed parameters are considered in area-2. The disturbed AVR system's parameters are $T_a = 0.1$, $K_a = 10$, $T_e = 0.6$, $K_e = 1.5$, $T_n = 1.5$, $K_n = 1.5$, $T_s = 0.01$ and $K_s = 1$, whereas the disturbed LFC system's parameters are $K_l = 100$, $T_l = 10$, $T_t = 0.15$, $T_g = 0.12$, and $R = 1.2$. An SLP of 2% is applied in both areas. The synchronization coefficient is taken as 0.545. The convergence curve for the four techniques is seen in Fig. 15. By evaluating the efficacy of the GBO method to that of ChOA, WOA, and GTO, it is possible to prove that the GBO algorithm has outstanding convergence over other algorithms. The resultant ITAE from the GBO algorithm is 0.03.

4.1.1. Case I: Tuning the AVR system individually

In this case, under the umbrella of two conditions for the AVR system's parameters (i.e., nominal and disturbed), The performance of the proposed GBO-optimized FPIDD^2 controller is compared to the performance of different controllers, such as the GBO-optimized FPID and the conventional PID controller optimized by the MONLTA technique (Nahas et al., 2021).

(a) Under nominal parameters

In this part, Individually, the AVR system is investigated using the nominal parameters listed in Table 1. The step response of the AVR system's output terminal voltage is depicted in Fig. 16, demonstrating the efficiency of the suggested controller over the other comparative controllers. Fig. 16 depicts a quick voltage rise to the reference value with a small overshooting amplitude and settling time. Table 8 shows the settings of the three comparative controllers, while Table 9 shows the dynamic AVR system performance, which clearly shows that the ITAE obtained by the

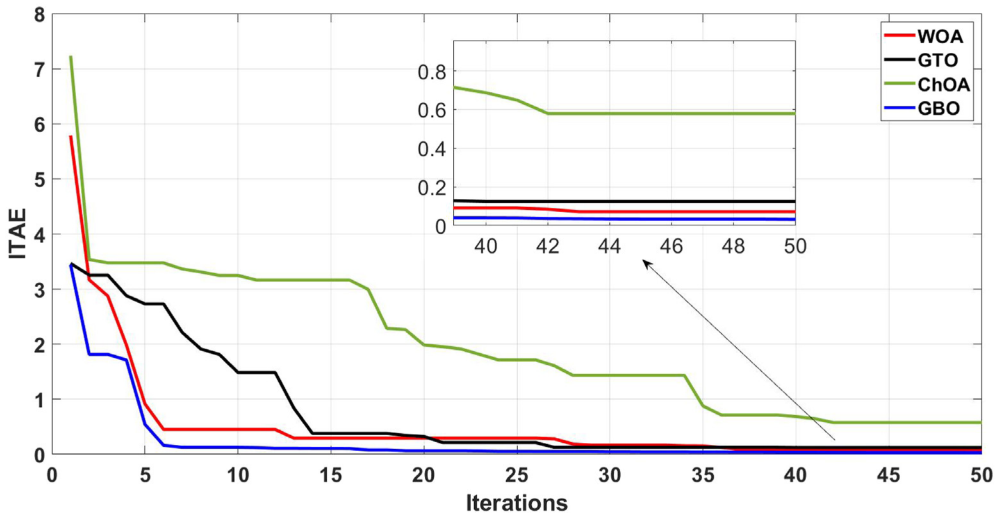

Fig. 15. Convergence curves of (ChOA, WOA, GBO) Algorithms.

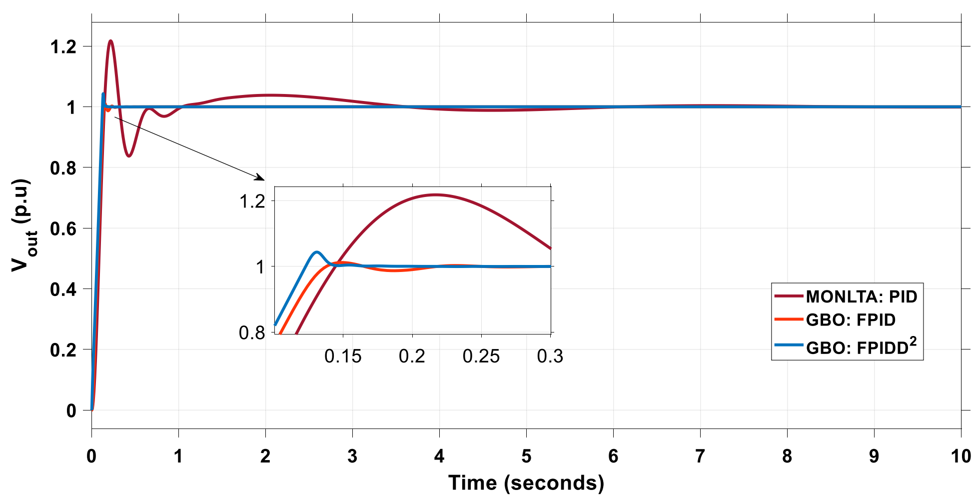

Fig. 16. The output voltage step response considering nominal parameters of the AVR system.

Table 8
The Optimum settings of the controllers in Case I under nominal case.

Controller	Controller parameters							
	K_P	K_I	K_{D1}	N_1	K_{D2}	N_2	K_1	K_2
PID tuned by MONLTA (Nahas et al., 2021)	0.889	1.714	0.882	–	–	–	–	–
FPID tuned by GBO	4	2.837	1.201	499.62	–	–	0.399	0.1
FPIDD^2 tuned by GBO (proposed)	3.998	2.587	1.715	499.89	0.023	499.71	1.329	0.1

Table 9
The AVR system dynamics as a consequence of Case I impact under nominal case.

Controller	M_p	τ_s	τ_r	τ_p	ITAE
PID tuned by MONLTA	1.218	0.56	0.098	0.218	0.2383
FPID tuned by GBO	1.0116	0.132	0.096	0.149	0.00325
FPIDD^2 tuned by GBO (proposed)	1.043	0.117	0.1	0.131	0.00277

suggested controller is the smallest one compared to the other controllers.

(b) Under disturbed parameters

Using a slight fluctuation in AVR system parameters around the nominal values, the influence of AVR dynamical system uncertainty on the quality of optimum settings determined by the optimization methodologies is depicted. The disturbed AVR system's parameters are $T_a = 0.1$, $K_a = 10$, $T_e = 0.6$, $K_e = 1.5$, $T_n = 1.5$, $K_n = 1.5$, $T_s = 0.01$ and $K_s = 1$. It is shown in Fig. 17 that the AVR system's output voltage step response is more efficient than the output voltage of the other controllers. As shown in Table 10, the dynamic AVR system performance reveals

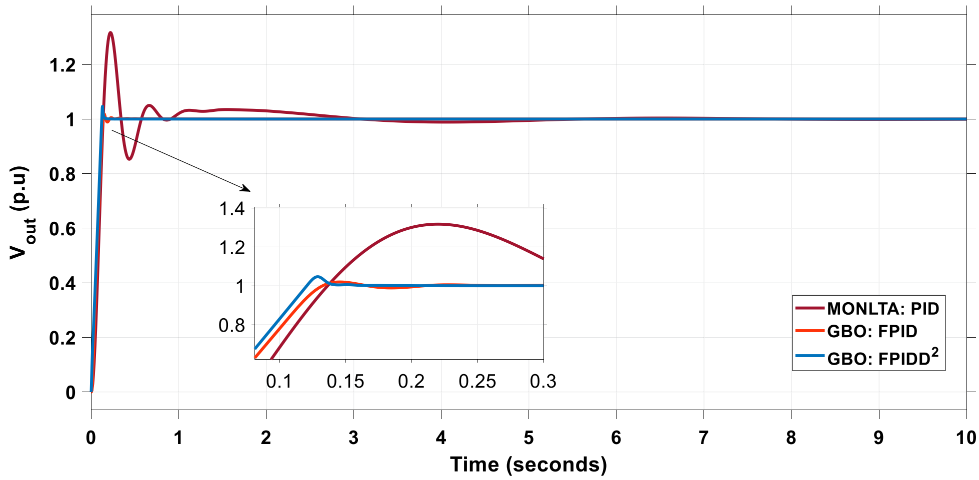

Fig. 17. The output voltage step response considering disturbed parameters of the AVR system.

Table 10
The AVR system dynamics as a consequence of Case I impact under disturbed case.

Controller	M_p	τ_s	τ_r	τ_p	ITAE
PID tuned by MONLTA	1.317	0.534	0.092	0.221	0.2996
FPID tuned by GBO	1.02	0.124	0.095	0.146	0.00388
FPIDD^2 tuned by GBO (proposed)	1.047	0.115	0.099	0.129	0.00279

Table 11
The Optimum settings of the controllers in Case II under nominal case.

Controller	Controller parameters							
	K_P	K_I	K_{D1}	N_1	K_{D2}	N_2	K_1	K_2
PID tuned by MONLTA	2.19	4	0.4334	–	–	–	–	–
FPID tuned by GBO	1.767	3.981	0.1811	500	–	–	3.992	0.4852
FPIDD^2 tuned by GBO (proposed)	1.648	3.921	0.146	465	0.023	499	3.792	0.001

Table 12
The LFC system dynamics as a consequence of Case II impact under nominal case.

Controller	ΔF (Hz)			ITAE
	MO	MU	ST	
PID tuned by MONLTA	0.0003	−0.0708	1.5	0.007
FPID tuned by GBO	0.0011	−0.0085	0.4	2.8×10^{-5}
FPIDD^2 tuned by GBO (proposed)	0.00003	−0.007	0.13	1.06×10^{-5}

that the proposed controller's reaction is unaffected by changes in any of the system parameters. The suggested controller's ITAE is nearly identical to the nominal case.

4.1.2. Case II: Tuning the LFC system individually

Like the AVR system, the LFC system has been investigated individually under two different conditions (nominal and disturbed) in order to validate the superiority of the suggested controller (FPIDD^2) over the other comparative controllers (i.e., MONLTA-tuned PID and GBO-tuned FPID).

(a) Under nominal parameters

The LFC system is studied in this section, considering the nominal parameters indicated in Table 2. Fig. 18 is a representation of the frequency variation caused by 10% SLP injection into the LFC system. This figure depicts the capability of the proposed controller to provide appropriate system stability and considerably lessen the impact of system fluctuation compared to the other controllers. The optimum setups of the three comparative controllers are detailed in Table 11, and the performance of the dynamic LFC system is presented in Table 12. It is abundantly obvious from this table that the recommended regulator achieved the lowest overshoot, undershoot, settling time, and ITAE values.

(b) Under disturbed parameters

Herein, a disturbed version of the LFC system is investigated for the purpose of testing the sensitivities of three comparative controllers to changes in system parameters in order to demonstrate the superiority of the controller that has been presented (FPIDD^2). The disturbed LFC system's parameters are $K_l = 100$, $T_l = 10$, $T_t = 0.15$, $T_g = 0.12$, and $R = 1.2$. Fig. 19 demonstrates that the frequency deviation that occurs under the management of the recommended regulator is nearly identical to that which occurs in the normal case. Furthermore, in contrast to other regulators, the ITAE that occurs under the suggested regulator's control is the lowest. The performance of the dynamic LFC system is displayed in Table 13, and it demonstrates that the reaction of the suggested controller is nearly unaffected by the changes in any of the system parameters. There has been no alteration in the maximum overshooting or undershooting, but there has been a tiny rise in the settling time, which has pushed the ITAE to 4.5×10^{-5}.

4.1.3. Case III: Tuning of combined LFC-AVR system

To confirm the exceptional performance of the recommended FPIDD^2 in the enhancement of voltage and frequency stability, this section makes use of the combined LFC-AVR scheme of the dual-area that was described earlier in Fig. 1 in which the nominal

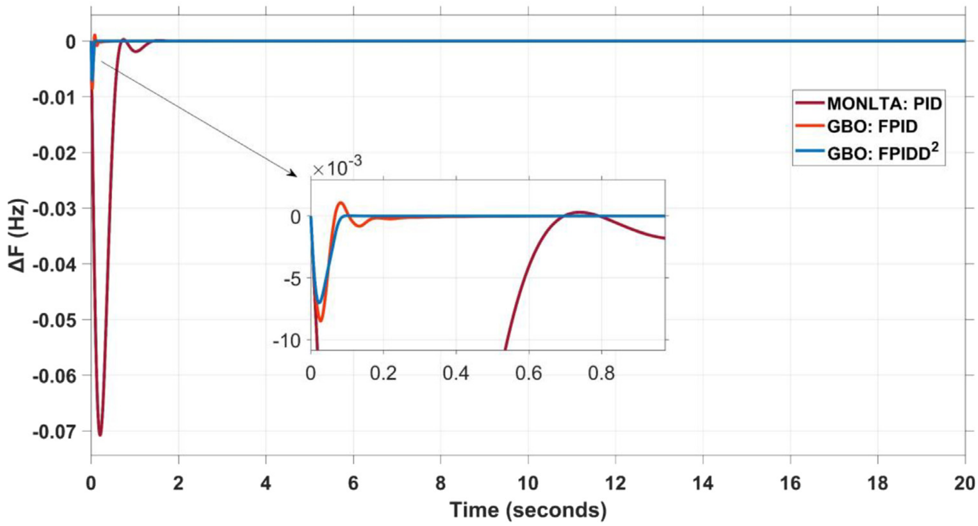

Fig. 18. The frequency deviation considering nominal parameters of the LFC system.

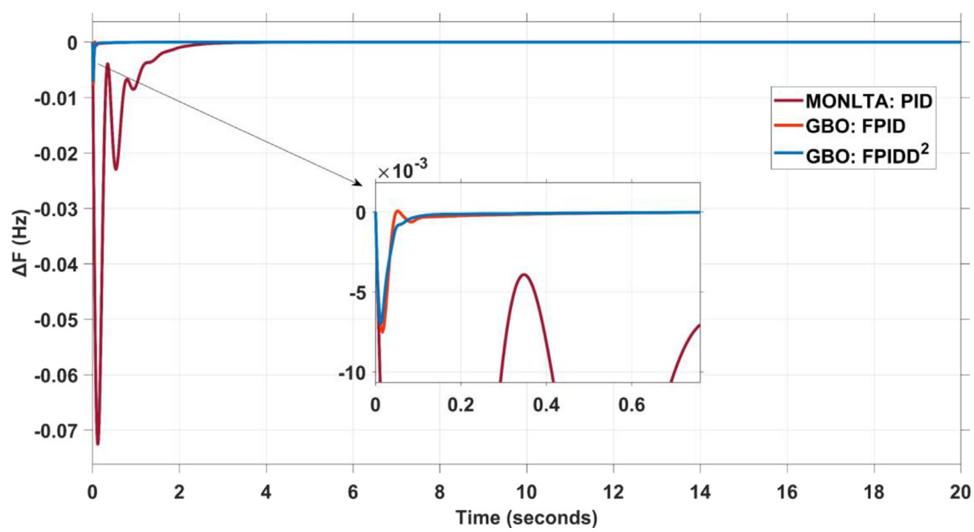

Fig. 19. The frequency deviation considering disturbed parameters of the LFC system.

Table 13
The LFC system dynamics as a consequence of Case II impact under disturbed case.

Controller	ΔF (Hz)			ITAE
	MO	MU	ST	
PID tuned by MONLTA	0	−0.0725	3	0.0122
FPID tuned by GBO	0	−0.0075	1	0.0001
FPIDD^2 tuned by GBO (proposed)	0	−0.0069	0.7	4.5×10^{-5}

values for the parameters of AVR and LFC systems are employed in area-1, whereas the disturbed parameters of AVR and LFC systems are applied in area-2. The investigation has been partitioned into two distinct scenarios, which are as follows:

(a) Normal scenario

In this scenario, unit-step references for the output terminal voltages are used ($V_{Ref.1} = V_{Ref.2} = 1$ p.u) and a 2% SLP is applied in both areas ($\Delta P_{d1} = \Delta P_{d2} = 0.02$ p.u). The synchronization coefficient between the two areas equals 0.545 ($C12 = 0.545$). Fig. 20 depicts the combined LFC-AVR system's performance under the effects of the preceding circumstances. The optimum configurations of the three controllers under comparison (PID, FPID, and FPIDD^2) are listed in Table 14, and the combined LFC-AVR system dynamics are provided in Table 15, in which the GBO-optimized FPIDD^2 has accomplished the lowest settling time for voltage and frequency responses and obtained an ITAE of 0.03 with an enhancement of 93.2% compared to the MONLTA-optimized PID controller and 77.78% compared to the GBO-tuned FPID controller.

(b) Disturbed scenario

This challenging scenario puts the three comparative controllers' resilience to the test since it considers time-varying required output voltages, random load perturbations, and time-varying synchronization coefficient as depicted in Figs. 20 to 22. Fig. 24 demonstrates the combined LFC-AVR system's response to this complicated control situation employing different control methodologies (i.e., FPIDD^2 and FPID controllers based on the GBO, and PID controller based on the MONLTA Nahas et al.,

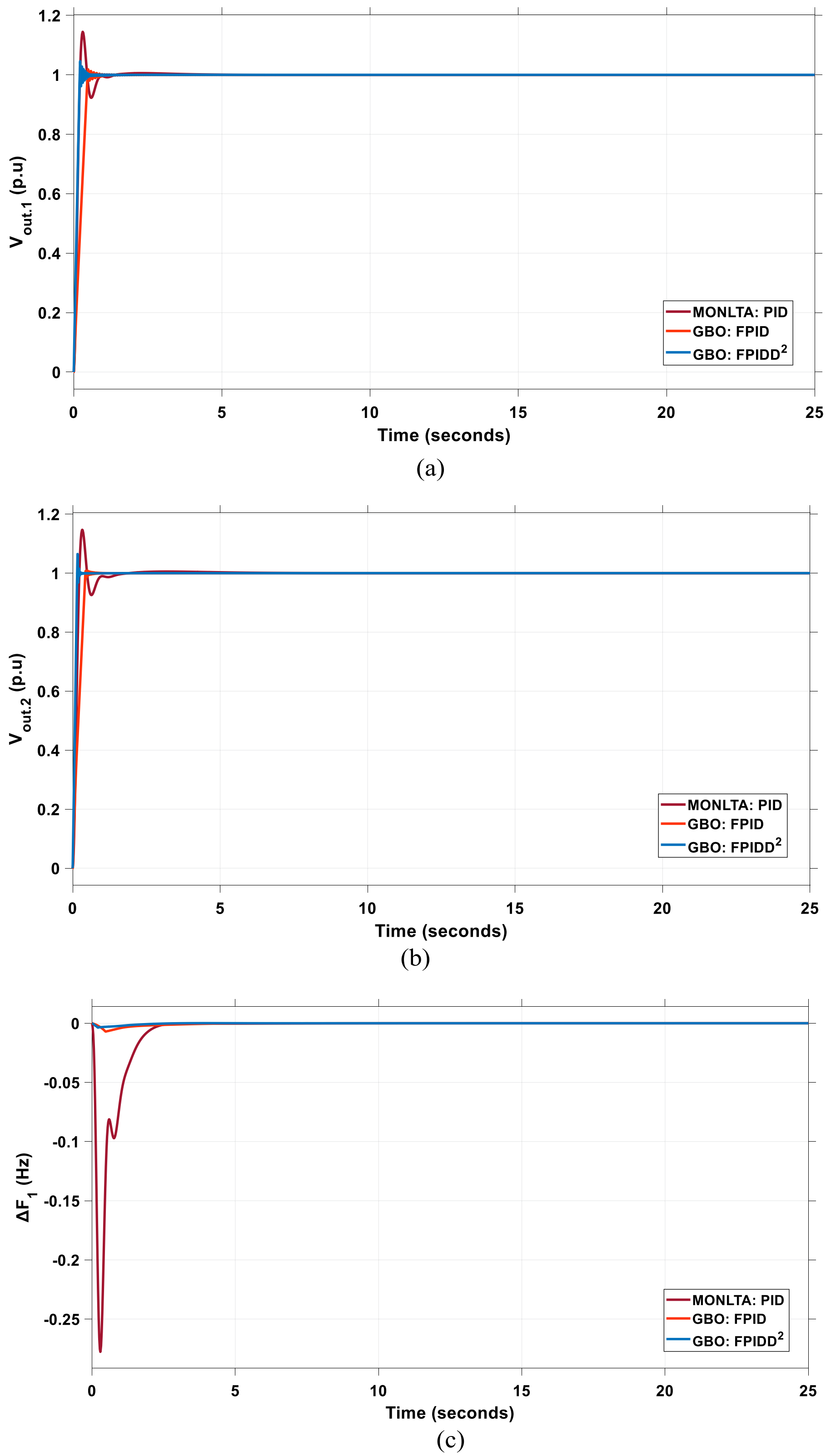

Fig. 20. Dynamic power system response for Case III under the normal scenario - (a) Vout1, (b) Vout2, (c) ΔF1, (d) ΔF2, (e) ΔPtie.

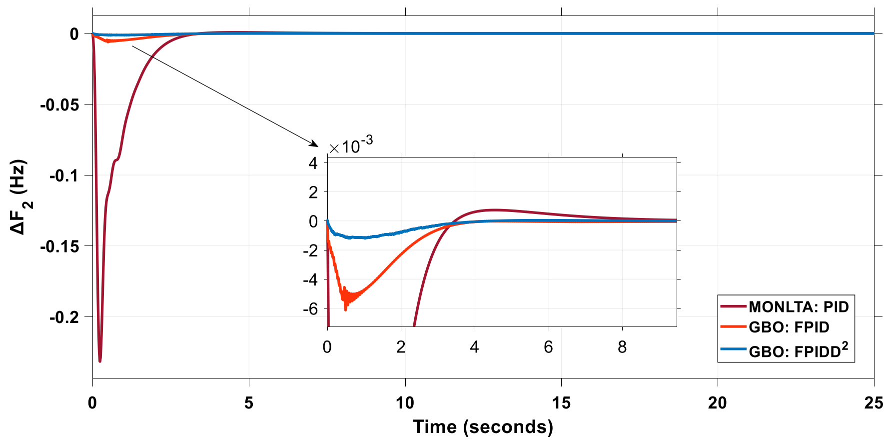

(d)

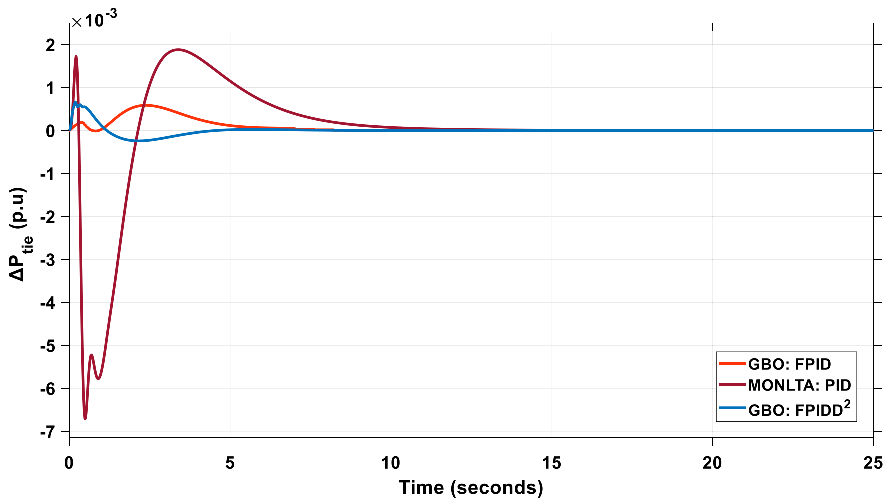

(e)

Fig. 20. (*continued*).

Table 14
The Optimum settings of the controllers in Case III under the normal scenario.

Controller	Area.1															
	AVR								LFC							
	K_P	K_I	K_{D1}	N_1	K_{D2}	N_2	K_1	K_2	K_P	K_I	K_{D1}	N_1	K_{D2}	N_2	K_1	K_2
PID tuned by MONLTA (Nahas et al., 2021)	2.241	1.563	0.997	–	–	–	–	–	2.427	2.487	0.916	–	–	–	–	–
FPID tuned by GBO	1.363	0.831	0.714	375	–	–	2.868	0.348	2.845	2.131	0.64	384	–	–	1.706	3.891
FPIDD^2 tuned by GBO (proposed)	1.876	1.676	1.832	425	0.007	500	2.782	0.152	1.98	1.573	1.165	322	0.002	496	3.971	2.92
Controller	Area.2															
	AVR								LFC							
	K_P	K_I	K_{D1}	N_1	K_{D2}	N_2	K_1	K_2	K_P	K_I	K_{D1}	N_1	K_{D2}	N_2	K_1	K_2
PID tuned by MONLTA (Nahas et al., 2021)	1.336	0.62	0.897	–	–	–	–	–	2.496	2.495	0.742	–	–	–	–	–
FPID tuned by GBO	3.459	0.963	1.38	379	–	–	2.481	0.423	2.134	2.065	1.067	364	–	–	1.348	0.112
FPIDD^2 tuned by GBO (proposed)	1.79	0.859	1.575	490	0.019	496	2.501	0.103	1.982	1.99	0.013	366	0.05	357	3.99	2.374

Table 15
The combined LFC-AVR system dynamics as a consequence of Case III impact under the normal scenario.

Controller	ΔF_1 (Hz)			ΔF_2 (Hz)			ΔP_{tie} (Mw p.u)			$V_{out.1}$ (pu)			$V_{out.2}$ (pu)			ITAE
	MO	MU	ST	MO	MU	ST	MO	MU	ST	M_p	τ_r	τ_s	M_p	τ_r	τ_s	
PID tuned by MONLTA	0	−0.278	8	0.0007	−0.231	6	0.0019	−0.0007	10.6	1.145	0.15	0.7	1.147	0.15	0.75	0.441
FPID tuned by GBO	0	−0.007	6	0	−0.006	3.5	0.0006	0	7.8	1.018	0.37	0.45	1.009	0.34	0.41	0.135
FPIDD^2 tuned by GBO (proposed)	0	−0.0037	3	0	−0.001	3.5	0.0006	−0.0002	3.8	1.046	0.16	0.19	1.065	0.12	0.17	0.027

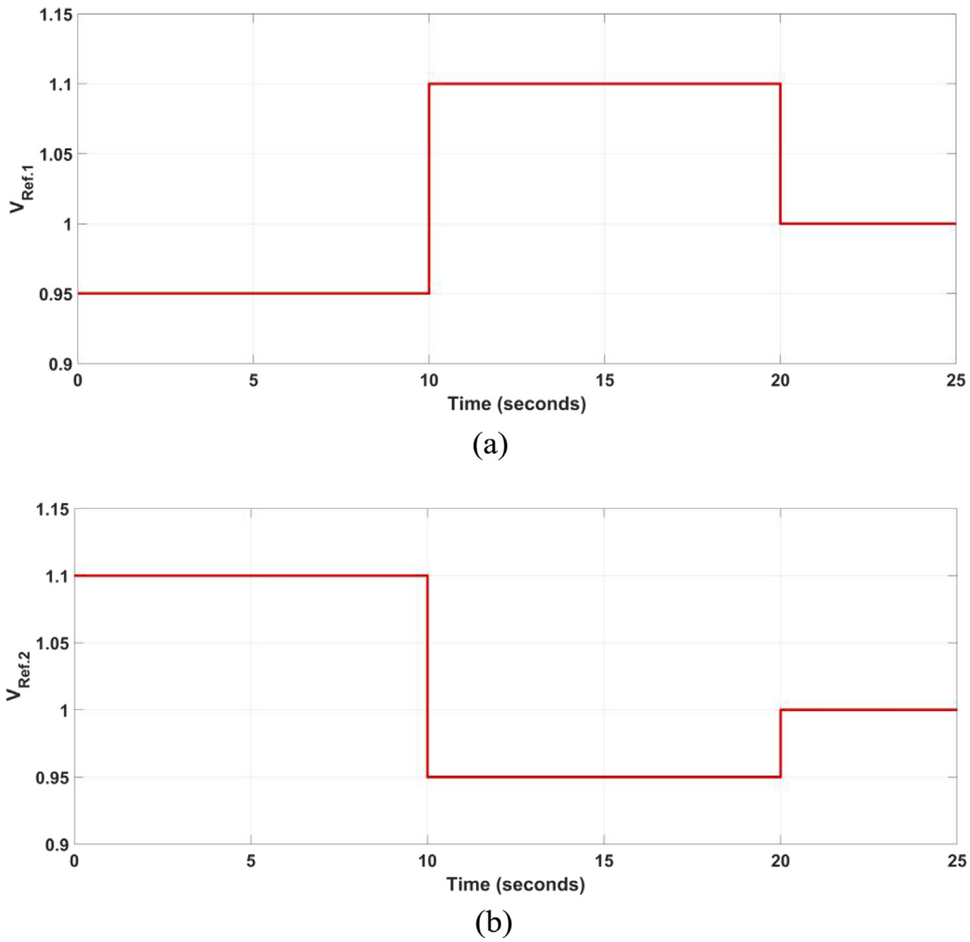

Fig. 21. The desired time-varying reference voltages for both areas-(a) Reference voltage for area-1, (b) Reference voltage for area-2.

Table 16
The combined LFC-AVR system dynamics as a consequence of Case III impact under the disturbed scenario represented by the ITAE index value.

Controller	ITAE					$ITAE_{total}$
	ΔF_1	ΔF_2	ΔP_{tie}	$V_{out.1}$	$V_{out.2}$	
PID tuned by MONLTA	3.454	2.663	1.722	0.7568	0.9073	9.503
FPID tuned by GBO	0.4011	0.3323	0.3107	0.3038	0.1722	1.5201
$FPIDD^2$ tuned by GBO (proposed)	0.0913	0.08	0.0326	0.2167	0.0817	0.5023

2021). Table 16 summarizes the dynamic performance of the system in terms of ITAE values for output voltages, frequency deviations, and tie-line power. In comparison to the MONLTA-tuned PID and the GBO-tuned FPID controllers, the GBO-tuned $FPIDD^2$ controller has the smallest rising and settling times. The suggested $FPIDD^2$ regulator reduces the frequency oscillations relatively fast, in addition to improved control quality, despite coping with rapid and gradual load fluctuations. The total ITAE value of the $FPIDD^2$ regulator tuned using the GBO approach was boosted by 94.79% with the MONLTA-based PID and 67.42% with GBO-based FPID controllers (see Fig. 23).

4.2. The hybrid system cases

4.2.1. Case I: Applying an MSLP in area 1 with the consideration of RESs penetration

The examined hybrid system's combined LFC and AVR model was investigated using several regulators such as classic ID-T and intelligent-based fuzzy PID and $PIDD^2$ in both LFC and AVR loops via applying MSLP, as denoted in Fig. 25, in area-1. Additionally, a PV solar unit with a rating of 50 MW is inserted into area-1 after 250 s, and a wind farm unit with a rating of 70 MW is inserted into area-2 after 100 s. These RESs disturbances are previously presented in Figs. 3 and 5, respectively. The convergence curves of the three examined controllers are exhibited in Fig. 26, demonstrating the superiority of the suggested controller employing the GBO. The responses of the combined LFC-AVR system were analyzed in light of the criteria of maximum overshooting (MO) and undershooting (MU) for the LFC loop, and maximum overshoot magnitude (Mp), rising and settling times (τr, τs) for the AVR loop, as shown in Fig. 27. After studying the results in Fig. 27, we came to the conclusion that the $FPIDD^2$ minimized undershoots and overshoots much better than other controllers. Furthermore, the terminal voltages were swiftly reached with the GBO-tuned $FPIDD^2$ regulator. Table 17 lists the ID-T/FPID/$FPIDD^2$ controller parameters that were optimally obtained using the GBO approach. Table 18 shows that the responses approached the steady state faster with the $FPIDD^2$ controller compared with other controllers. As a result, the intelligent $FPIDD^2$ demonstrated

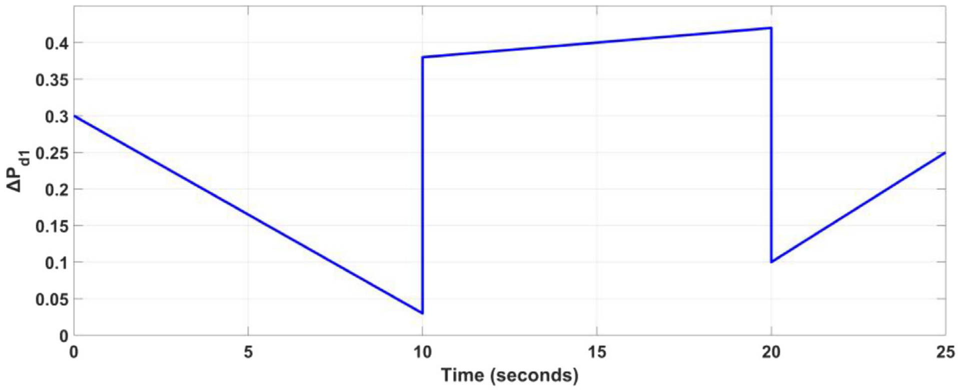

(a)

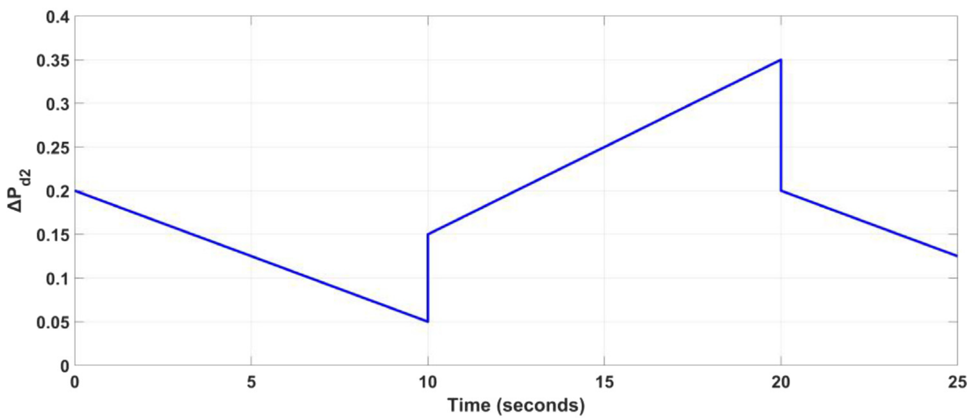

(b)

Fig. 22. The RLP injected in both areas-(a) The RLP injected in area-1, (b) The RLP injected in area-2.

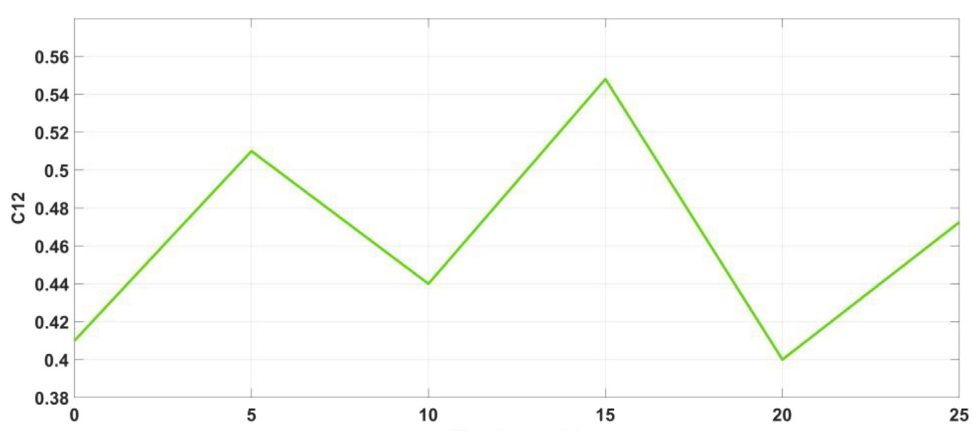

Fig. 23. The time-varying synchronization coefficient.

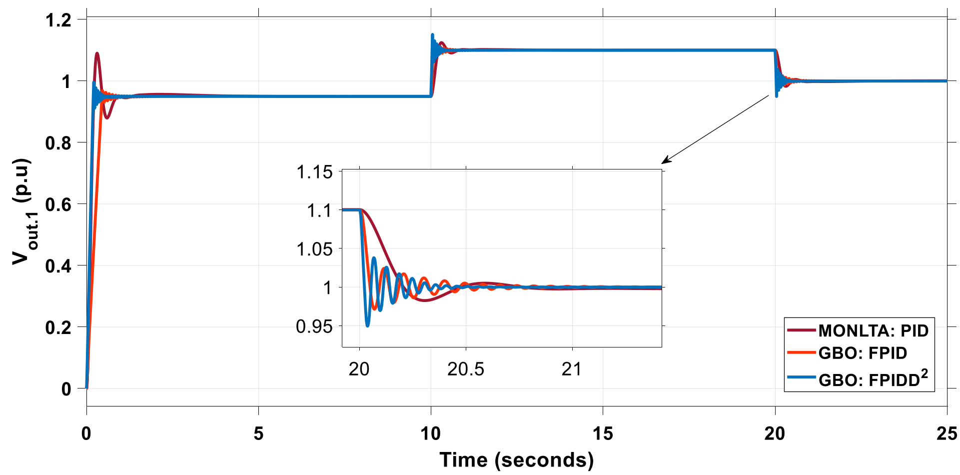

(a)

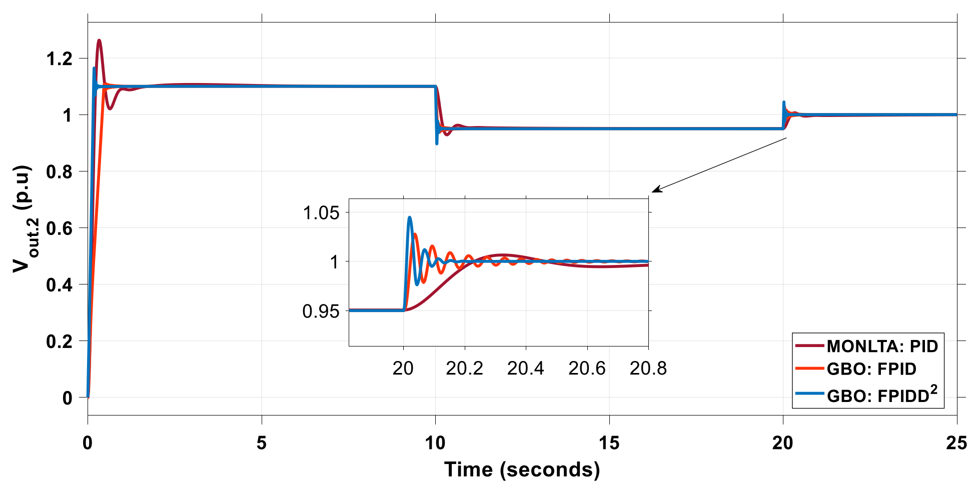

(b)

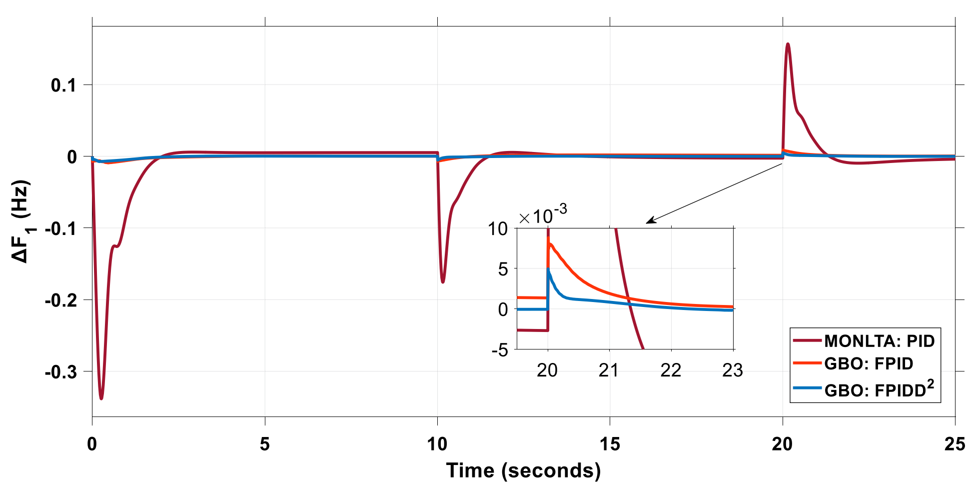

(c)

Fig. 24. Dynamic power system response for Case III under the disturbed scenario - (a) Vout1, (b) Vout2, (c) ⊿F1, (d) ⊿F2, (e) ⊿Ptie.

its superiority in managing the behavior of the complicated hybrid system of the LFC-AVR combination model. The ITAE value of the FPIDD^2 regulator tuned by the GBO technique was enhanced by 91.66% with the GBO-based ID-T and 56.96% with GBO-based FPID controllers.

4.2.2. Case II: Applying a CTD to the controller output with the consideration of RESs penetration

This case involves an endurance challenge during which RESs have been introduced into both areas of the power system that is being examined. The PV unit is inserted at 80 s while the wind

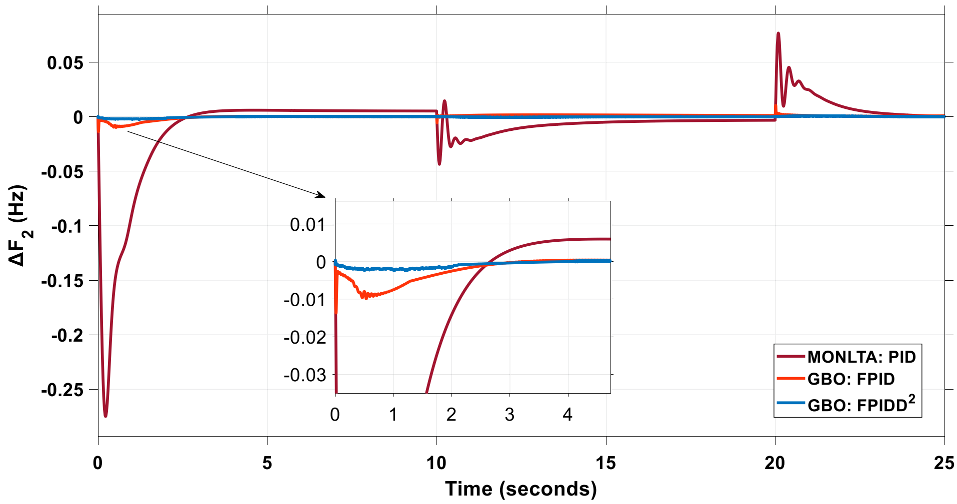

(d)

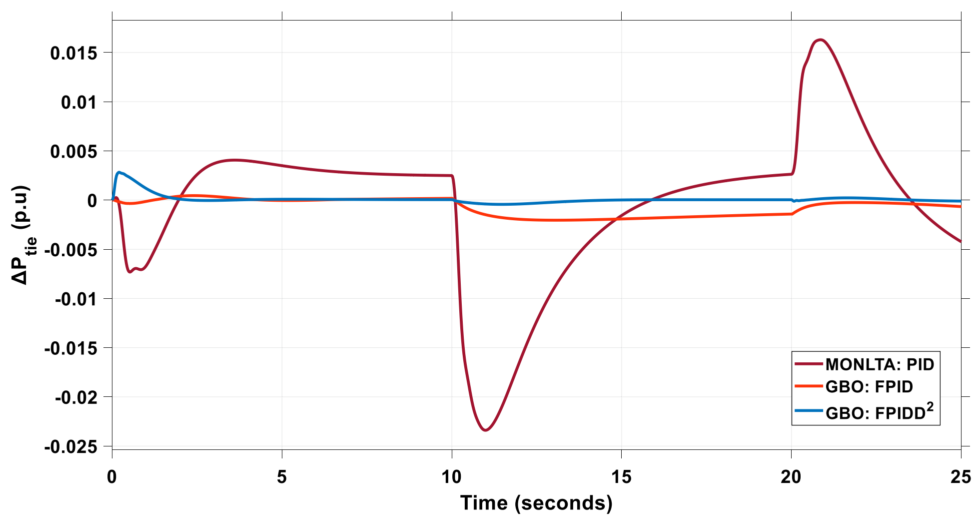

(e)

Fig. 24. (*continued*).

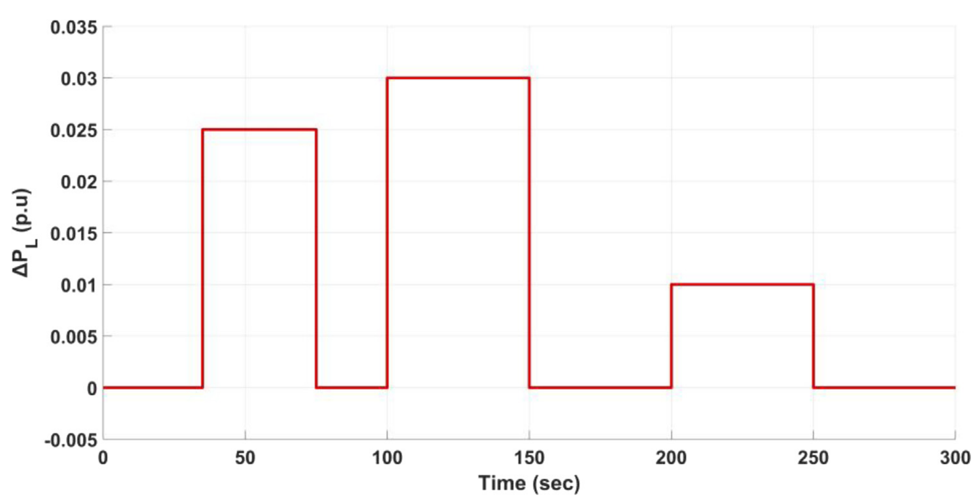

Fig. 25. The MSLP used in Case I.

unit is inserted at 220 s. Additionally, the injection of 1% SLP to area-1 at 10 s and 5% SLP to area-2 at 150 s. Furthermore, to test the efficacy and robustness of the controllers, a 0.1 s CTD is added to the controllers' output. Table 19 presents the settings of the three controllers (FPIDD^2, FPID, and ID-T) optimized by the GBO technique, and Table 20 displays the dynamic performance

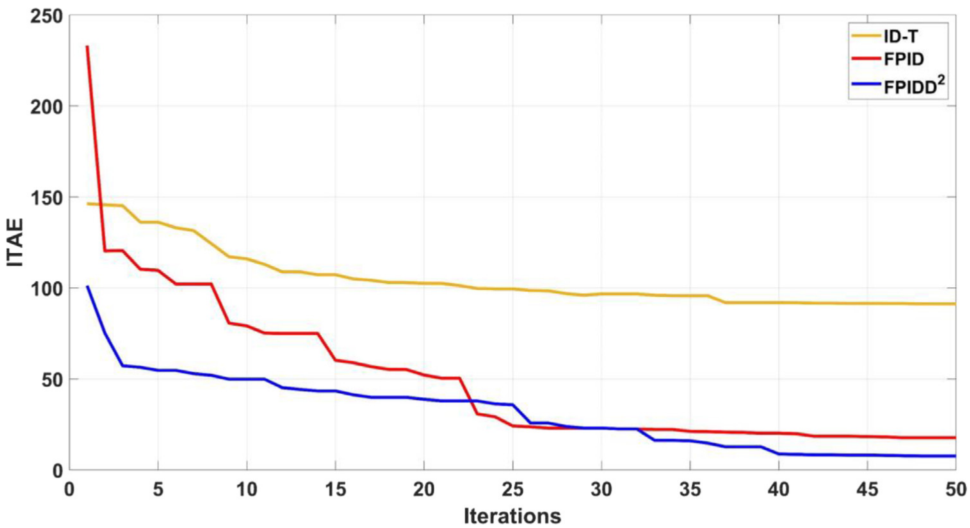

Fig. 26. The three controllers' convergence curves as a consequence of Case I impact.

Table 17
The Optimum settings of the controllers in Case I.

Controller	Area.1															
	AVR								LFC							
	K_P/K_T	K_I	K_{D1}	N_1	K_{D2}	N_2/n	K_1	K_2	K_P/K_T	K_I	K_{D1}	N_1	K_{D2}	N_2/n	K_1	K_2
ID-T tuned by GBO	1.575	9.98	2.218	496.6	–	9.955	–	–	0.007	0.230	10	314.7	–	8.689	–	–
FPID tuned by GBO	1.045	1.178	0.589	415.2	–	–	1.992	0.382	3.275	3.87	2.672	400.4	–	–	1.339	2.418
FPIDD^2 tuned by GBO (proposed)	0.422	3.371	0.345	495.9	0.006	463.2	0.83	3.362	3.831	3.714	3.07	472.1	0.031	474.8	3.523	2.658
Controller	Area.2															
	AVR								LFC							
	K_P/K_T	K_I	K_{D1}	N_1	K_{D2}	N_2/n	K_1	K_2	K_P/K_T	K_I	K_{D1}	N_1	K_{D2}	N_2/n	K_1	K_2
ID-T tuned by GBO	1.662	9.96	1.216	333.9	–	9.958	–	–	2.004	9.973	5.717	500	–	9.896	–	–
FPID tuned by GBO	1.16	1.645	0.22	438.2	–	–	1.428	1.333	3.701	3.953	1.459	435.6	–	–	1.909	1.334
FPIDD^2 tuned by GBO (proposed)	1.305	0.147	0.136	471.7	0.001	450	3.764	3.515	1.587	3.113	0.251	464.3	0.047	452.3	3.736	3.981

Table 18
The system dynamics as a consequence of Case I impact.

Controller	ΔF_1 (Hz)		ΔF_2 (Hz)		ΔP_{tie} (Mw p.u)		$V_{out.1}$ (pu)			$V_{out.2}$ (pu)			ITAE
	MO	MU	MO	MU	MO	MU	M_p	τ_r	τ_s	M_p	τ_r	τ_s	
ID-T tuned by GBO	0.112	−0.711	0.213	−0.778	0.023	−0.046	1.279	0.076	5.8	1.109	0.14	5.08	91.21
FPID tuned by GBO	0.016	−0.095	0.019	−0.063	0.001	−0.006	1	2.7	3.5	1	2.44	2.83	17.68
FPIDD^2 tuned by GBO (proposed)	0.004	−0.018	0.018	−0.061	0.005	−0.002	1.007	0.43	0.5	1.001	1.19	1.44	7.61

of the system in this case. Fig. 28 depicts the three controllers' convergence curves. Both the voltage response and the frequency variation of both areas of the power system network that were analyzed are depicted in Fig. 29, together with the flow of power in the tie-line. The behavior of the system has significantly wavered as a result of disruptions caused by RES sources and the use of a communication time delay. On the other hand, the FPIDD^2 regulator that was recommended can achieve enough stability for the system power network and considerably lessen the impact of system fluctuations. After analyzing the data in Fig. 29, we observed that the FPIDD^2 suppressed undershoots and overshoots in frequency deviations significantly better than other controllers. Furthermore, the GBO-tuned FPIDD^2 regulator quickly achieved the reference terminal voltage with a small peak overshoot and settling time. The ITAE index value of the FPIDD^2 regulator tuned by the GBO technique was enhanced by 39.09% with the GBO-based ID-T and 35.28% with the GBO-based FPID controllers.

4.2.3. Case III: Applying an RLP in area 1 as well as a time-varying desired output voltage with the consideration of RESs penetration

In this particular scenario, the researched system dynamics are analyzed in the presence of significant perturbations to corroborate the reliability and dominance of the FPIDD^2 controller that was recommended. To begin, random load perturbations, which are depicted in Fig. 30, are implemented in area-1, which may be portrayed by a series of industrial loads connected to a power system network. Moreover, the penetrations of RESs that are depicted in Figs. 5 and 7 are represented by the connection of the photovoltaic unit to area-1 and the wind unit to area-2 after time intervals of 250 and 100 s respectively. Furthermore, both areas require the time-varying reference voltages indicated in Fig. 31. Fig. 32 displays the system's response to this complex control case using multiple control strategies (i.e., FPIDD^2, FPID, and ID-T controllers based on the GBO). Table 21 provides a summary of the system's dynamic performance in the form of ITAE values for output voltages and deviations in frequency and tie-line power. Compared to the ID-T and FPID controllers, the

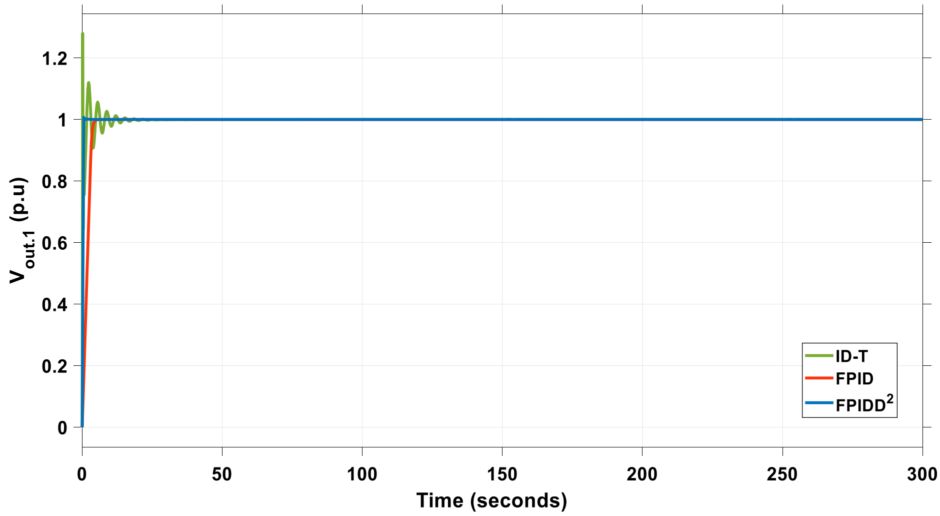

(a)

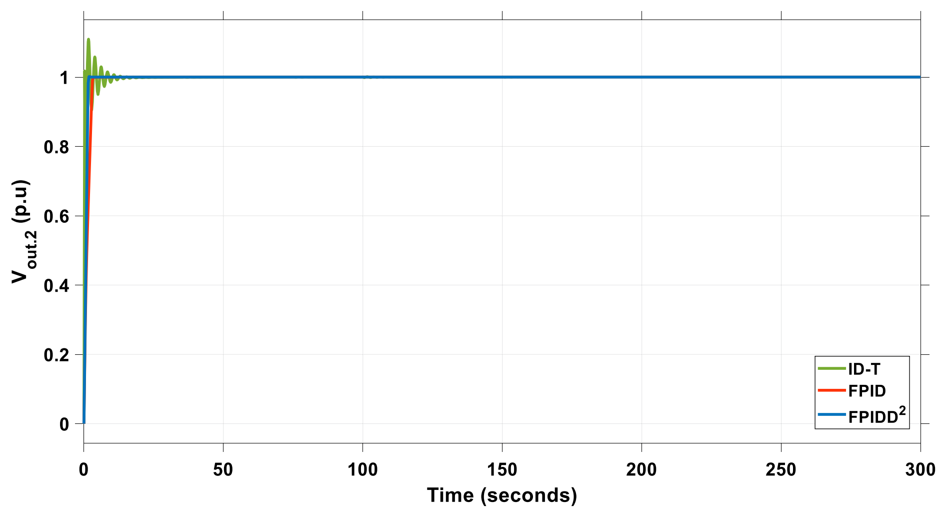

(b)

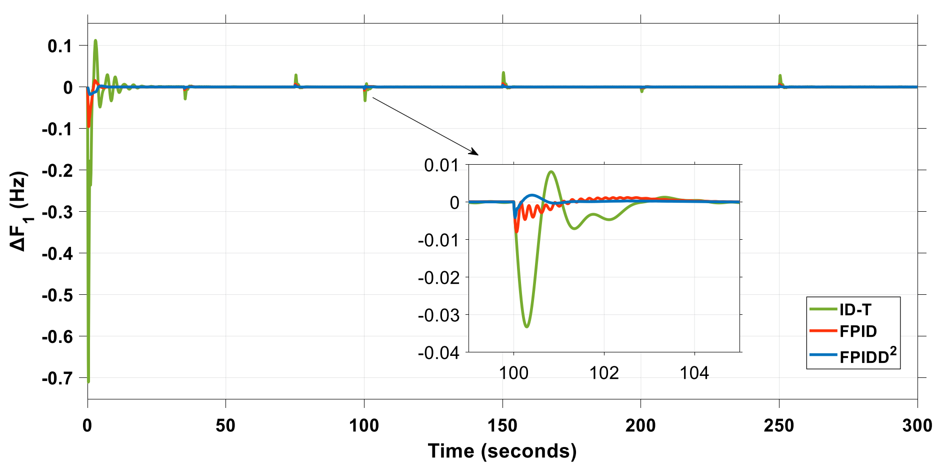

(c)

Fig. 27. Dynamic power system response for Case I - (a) Vout1, (b) Vout2, (c) ΔF1, (d) ΔF2, (e) ΔPtie.

suggested FPIDD^2 controller tuned by the GBO technique has the quickest reaction and the greater ability to quickly obtain the target voltage with a smaller steady-state error. And from the perspective of frequency stability, the recommended FPIDD^2 controller dampens oscillations extremely quickly, with the lowest undershooting and overshooting, in addition to superior control quality, while dealing with rapid and gradual load variations. The total ITAE value of the FPIDD^2 regulator tuned by the GBO technique was enhanced by 90.9% with the GBO-based ID-T and 55.4% with GBO-based FPID controllers.

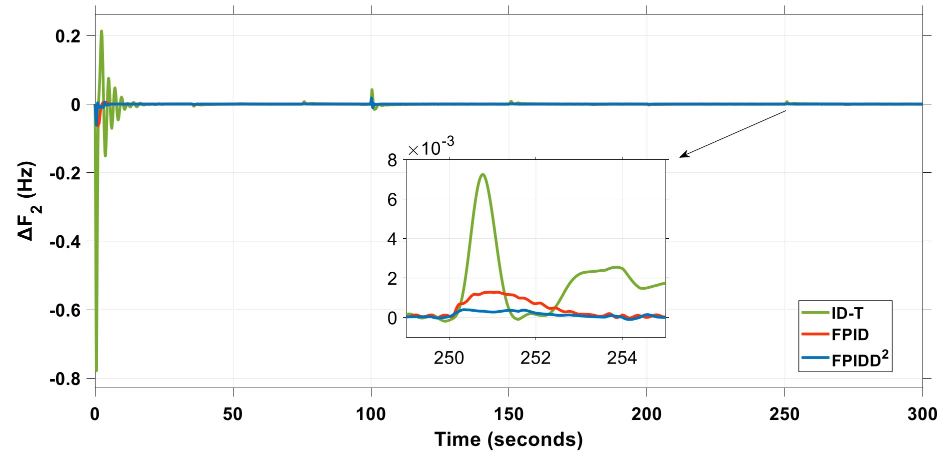

(d)

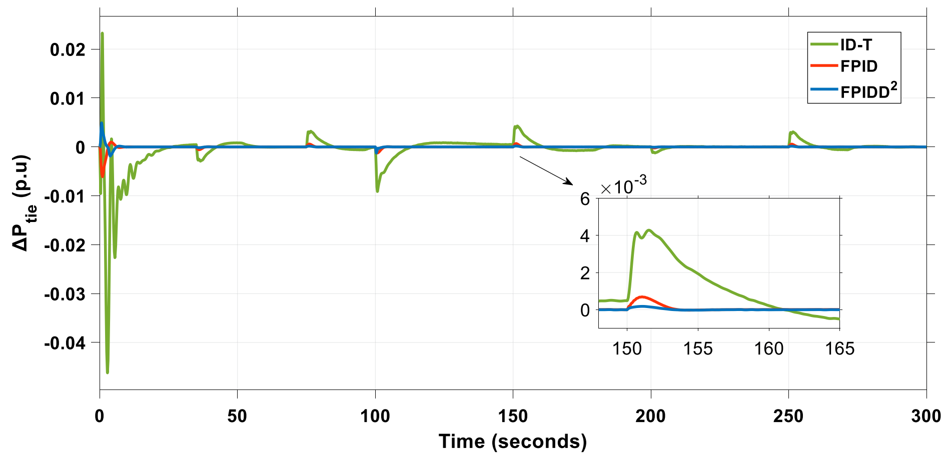

(e)

Fig. 27. (*continued*).

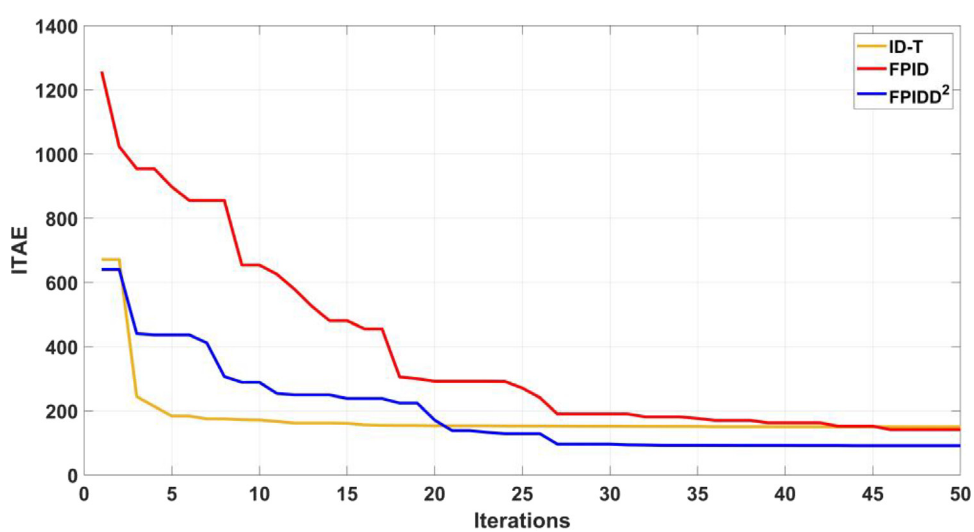

Fig. 28. The three controllers' convergence curves as a consequence of Case II impact.

4.2.4. Case IV: Sensitivity analysis with the consideration of RESs penetration

This case examines the FPIDD^2 performance when system parameters are changed by ±50%. The first region had 0.01 p.u step load penetration after 10 s and the second had 0.03 p.u after 150 s. PV solar and wind turbines are interlinked at 80 and 220 s. Table 17 provides the FPIDD^2 parameters for this case. Table 22 summarizes the power system dynamics. Fig. 33 shows the dynamic power system responses to a ±50% setting change. Based on the dynamical analysis results, it is probably fair to say that the FPIDD^2 regulator is resilient to variations in system model parameters and step load penetration.

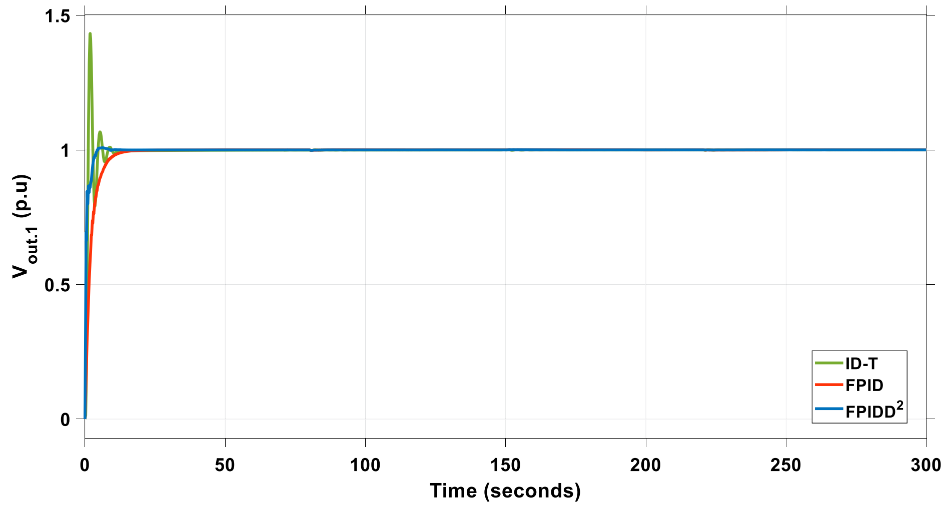

(a)

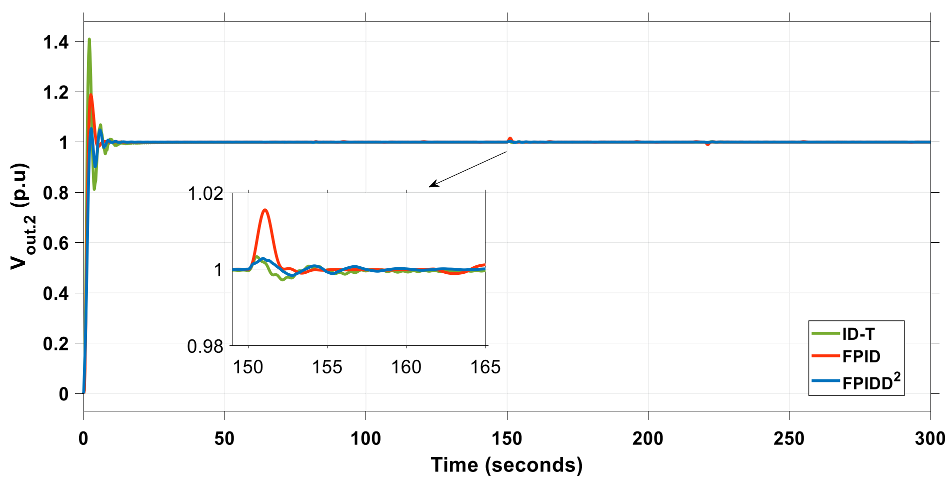

(b)

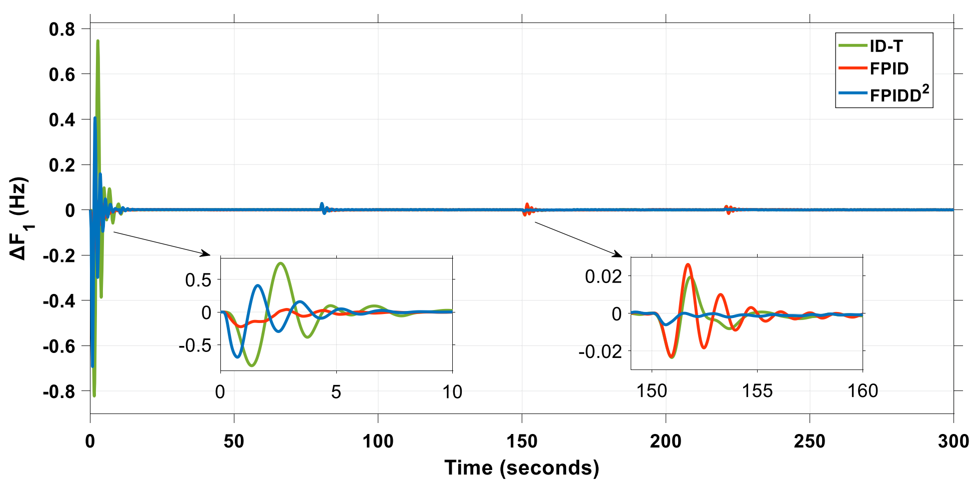

(c)

Fig. 29. Dynamic power system response for Case II - (a) Vout1, (b) Vout2, (c) ΔF1, (d) ΔF2, (e) ΔPtie.

5. Conclusion

Connecting the AVR loop with the LFC through the use of coupling coefficients allows for simultaneous attention to be paid to the stability of the voltage and frequency of the interconnected hybrid power system. In this research, the LFC and AVR loops were controlled by a GBO-tuned FPIDD^2 implemented as a secondary regulator. The dynamical study was widely performed on different two-area systems (conventional and hybrid). For the conventional system, the suggested FPIDD^2 proves to have great performance compared to the MONLTA-based PID and the GBO-based FPID controllers under numerous cases (i.e., tuning the

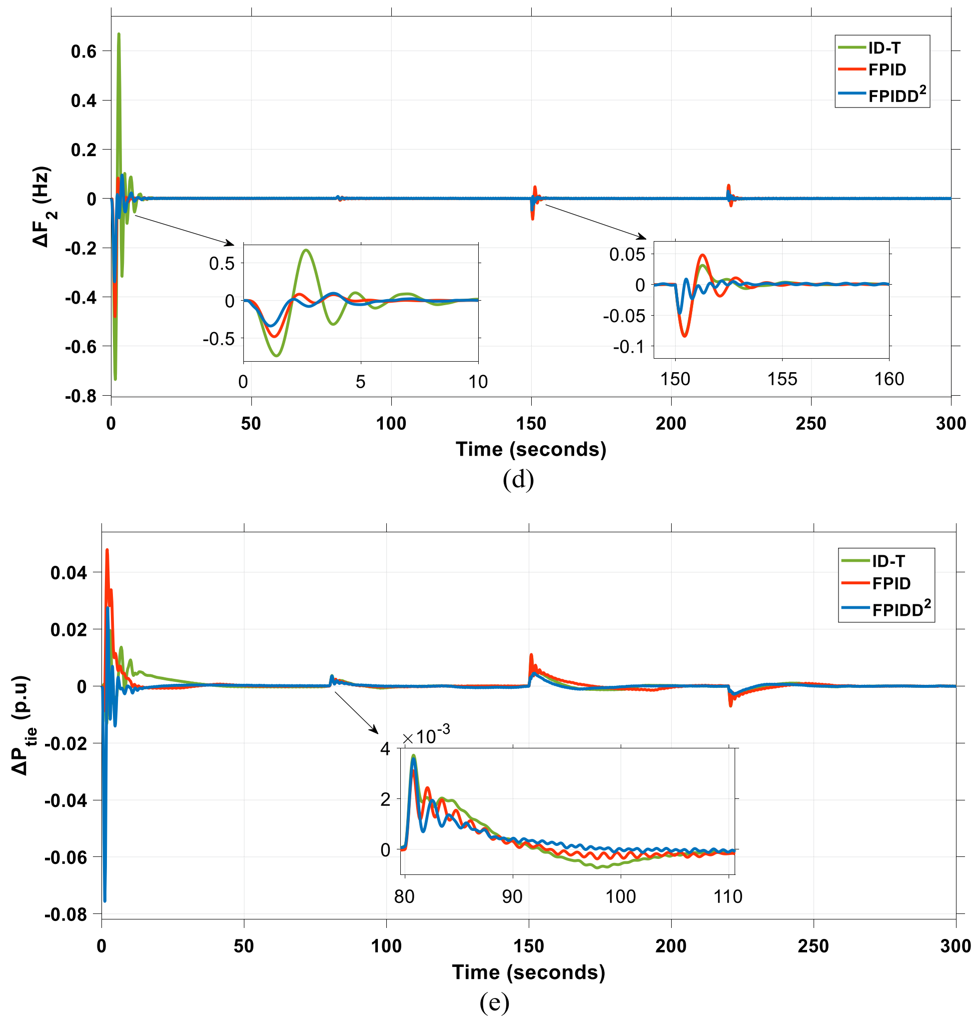

Fig. 29. (*continued*).

Table 19
The Optimum settings of the controllers in Case II.

Controller	Area.1															
	AVR								LFC							
	K_P/K_T	K_I	K_{D1}	N_1	K_{D2}	N_2/n	K_1	K_2	K_P/K_T	K_I	K_{D1}	N_1	K_{D2}	N_2/n	K_1	K_2
ID-T tuned by GBO	1.352	3.541	1.045	424	–	9.952	–	–	3.417	3.984	3.921	405	–	9.942	–	–
FPID tuned by GBO	0.205	0.057	0.048	300	–	–	0.158	1.941	0.225	0.254	0.355	302	–	–	0.44	0.531
FPIDD^2 tuned by GBO (proposed)	0.256	0.136	0.263	300.6	0.001	353.9	0.139	0.251	0.082	0.372	0.284	318.6	0.001	322.6	0.349	0.379
Controller	Area.2															
	AVR								LFC							
	K_P/K_T	K_I	K_{D1}	N_1	K_{D2}	N_2/n	K_1	K_2	K_P/K_T	K_I	K_{D1}	N_1	K_{D2}	N_2/n	K_1	K_2
ID-T tuned by GBO	1.279	3.188	1.106	500	–	9.967	–	–	2.655	0.64	3.244	423	–	9.998	–	–
FPID tuned by GBO	0.13	0.21	0.001	468.4	–	–	0.075	0.268	0.482	0.063	0.491	300.3	–	–	0.165	0.109
FPIDD^2 tuned by GBO (proposed)	0.002	0.345	0.05	312.2	0.001	300.2	0.203	1.261	1.674	1.912	0.937	342.6	0.005	300	0.201	1.965

Table 20
The system dynamics as a consequence of Case II impact.

Controller	ΔF_1 (Hz)		ΔF_2 (Hz)		ΔP_{tie} (Mw p.u)		$V_{out.1}$ (pu)			$V_{out.2}$ (pu)			ITAE
	MO	MU	MO	MU	MO	MU	M_p	τ_r	τ_s	M_p	τ_r	τ_s	
ID-T tuned by GBO	0.75	−0.82	0.67	−0.74	0.019	−0.013	1.43	0.66	5.8	1.41	0.76	6.2	150.08
FPID tuned by GBO	0.04	−0.225	0.083	−0.48	0.048	−0.009	1	5.31	7.6	1.19	1.04	3.93	141.24
FPIDD^2 tuned by GBO (proposed)	0.41	−0.69	0.076	−0.339	0.027	−0.076	1.008	2.18	2.8	1.054	1.58	4.7	91.41

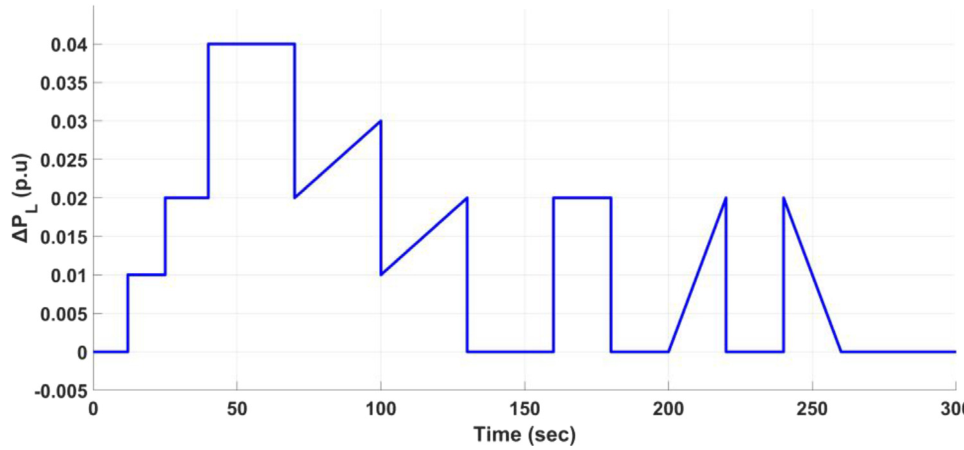

Fig. 30. The RLP used in Case III.

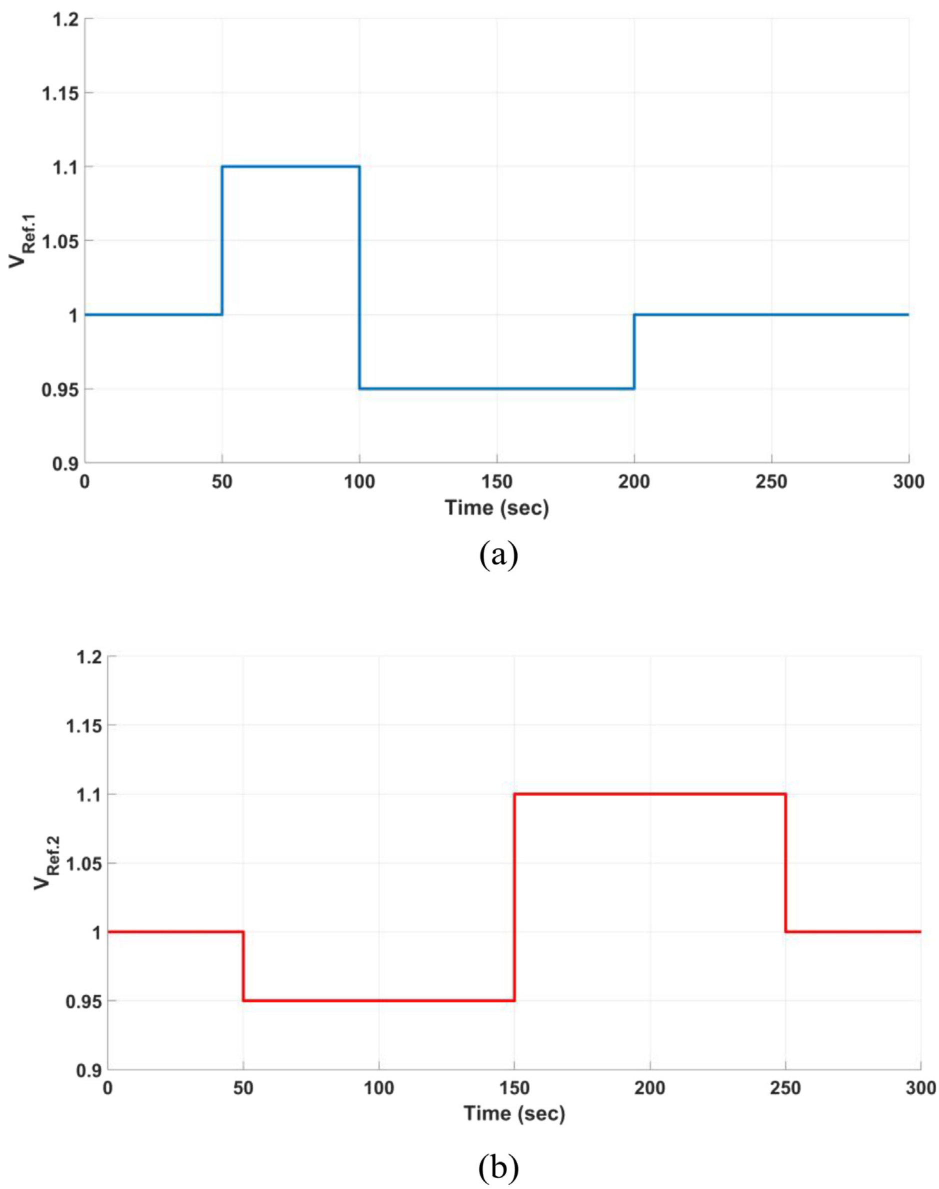

Fig. 31. The desired time-varying reference voltages for both areas-(a) Reference voltage for area-1, (b) Reference voltage for area-2.

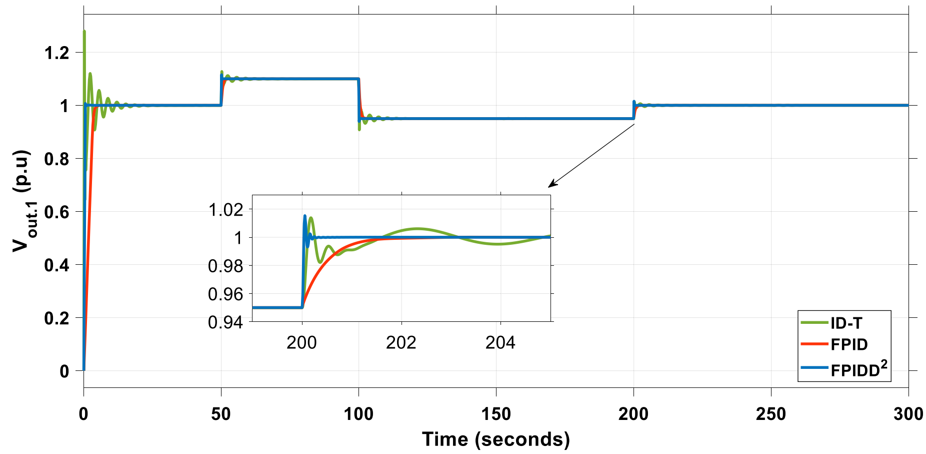

(a)

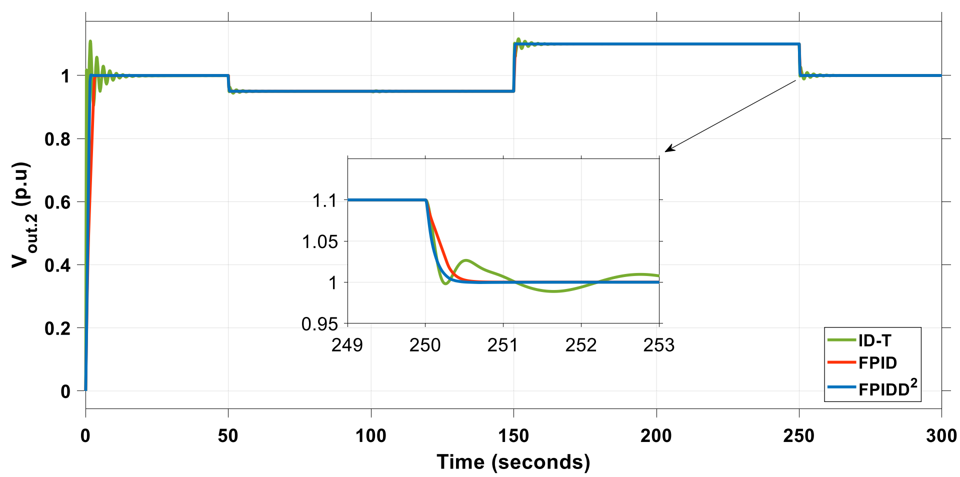

(b)

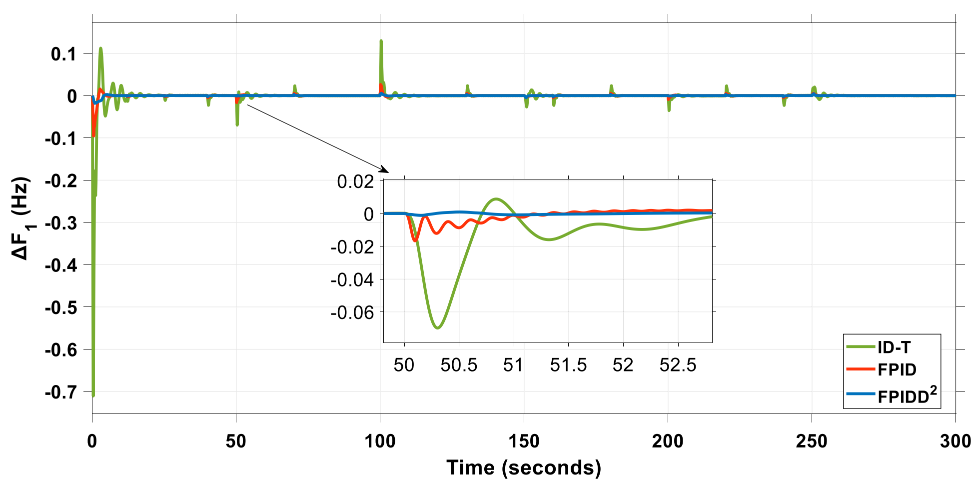

(c)

Fig. 32. Dynamic power system response for Case III - (a) Vout1, (b) Vout2, (c) ΔF1, (d) ΔF2, (e) ΔPtie.

Table 21
The system dynamics as a consequence of Case III impact represented by the ITAE index value.

Controller	ITAE					$ITAE_{total}$
	ΔF_1	ΔF_2	ΔP_{tie}	$V_{out.1}$	$V_{out.2}$	
ID-T tuned by GBO	63.23	84	56.17	32.41	37.07	272.88
FPID tuned by GBO	12.89	10.83	2.852	15.83	13.25	55.65
$FPIDD^2$ tuned by GBO (proposed)	5.233	10.17	1.346	1.475	6.601	24.82

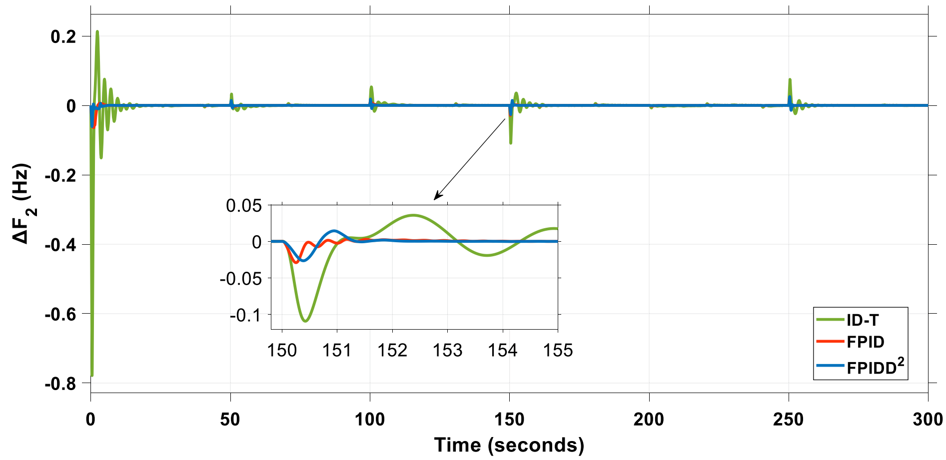

(d)

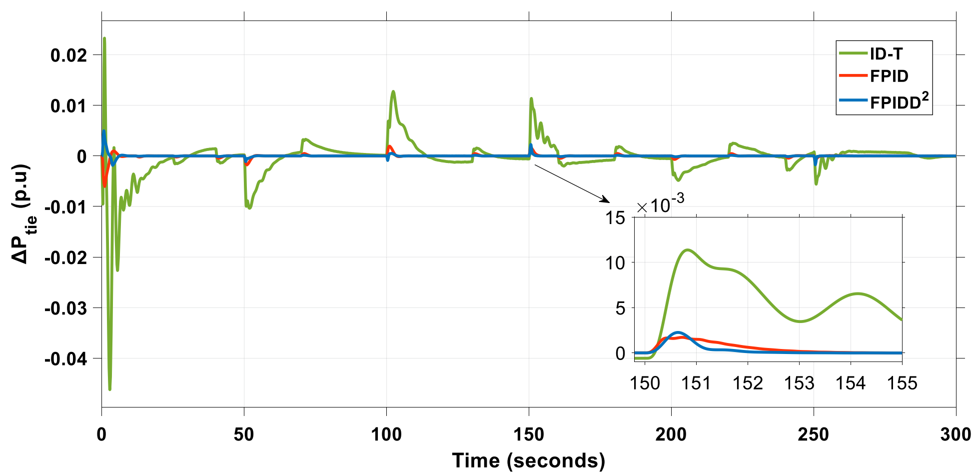

(e)

Fig. 32. (*continued*).

Table 22
The system dynamics as a consequence of Case IV impact.

Controller	Parameters variation	ΔF_1 (Hz)		ΔF_2 (Hz)		ΔP_{tie} (Mw p.u)		$V_{out.1}$ (pu)			$V_{out.2}$ (pu)			ITAE
		MO	MU	MO	MU	MO	MU	M_p	τ_r	τ_s	M_p	τ_r	τ_s	
FPIDD^2 tuned by GBO (proposed)	Nominal	0.0027	−0.018	0.0182	−0.061	0.005	−0.002	1.007	0.43	0.51	1.002	1.19	1.42	8.89
	+50%	0.0036	−0.012	0.0184	−0.063	0.0052	−0.002	1.007	0.43	0.51	1.002	1.19	1.42	8.92
	−50%	0.0026	−0.016	0.0177	−0.057	0.0044	−0.001	1.007	0.43	0.51	1.002	1.19	1.42	8.81

AVR and LFC systems individually or coupled) with nominal and disturbed system parameters. Additionally, the proposed FPIDD^2 regulator has demonstrated greater stability and robustness compared to the GBO-based ID-T/FPID controllers under the impact of different scenarios (i.e., the injection of multiple perturbations such as MSLP, RLP with time-varying desired output voltage, and the application of communication time delay to the controller output, and ±50% system parameters' variations considering RESs penetration for all scenarios) on the hybrid system. The responses of the combined LFC and AVR model demonstrate the superiority of FPIDD^2 over both the traditional ID-T and the intelligent FPID. Future research may investigate the impact of adding electric vehicles and energy storage devices to the hybrid system, and a four-area hybrid power system may be studied.

CRediT authorship contribution statement

Kareem M. AboRas: Conceptualization, Methodology, Investigation, Supervision, Formal analysis, Validation, Writing – original draft, Writing – review & editing. **Muhammad Ragab:** Methodology, Resources, Formal analysis, Writing – review & editing. **Mokhtar Shouran:** Methodology, Visualization, Resources, Funding acquisition, Writing – review & editing. **Sultan Alghamdi:** Data curation, Software, Validation, Writing – review & editing. **Hossam Kotb:** Conceptualization, Methodology, Investigation, Formal analysis, Supervision, Validation, Writing – original draft, Writing – review & editing.

Declaration of competing interest

The authors declare that they have no known competing financial interests or personal relationships that could have appeared to influence the work reported in this paper.

Data availability

Data will be made available on request.

Acknowledgment

This research work was funded by Institutional Fund Projects under grant no. (IFPIP:1379-135-1443). The authors gratefully acknowledge technical and financial support provided by the Ministry of Education and King Abdulaziz University, DSR, Jeddah, Saudi Arabia.

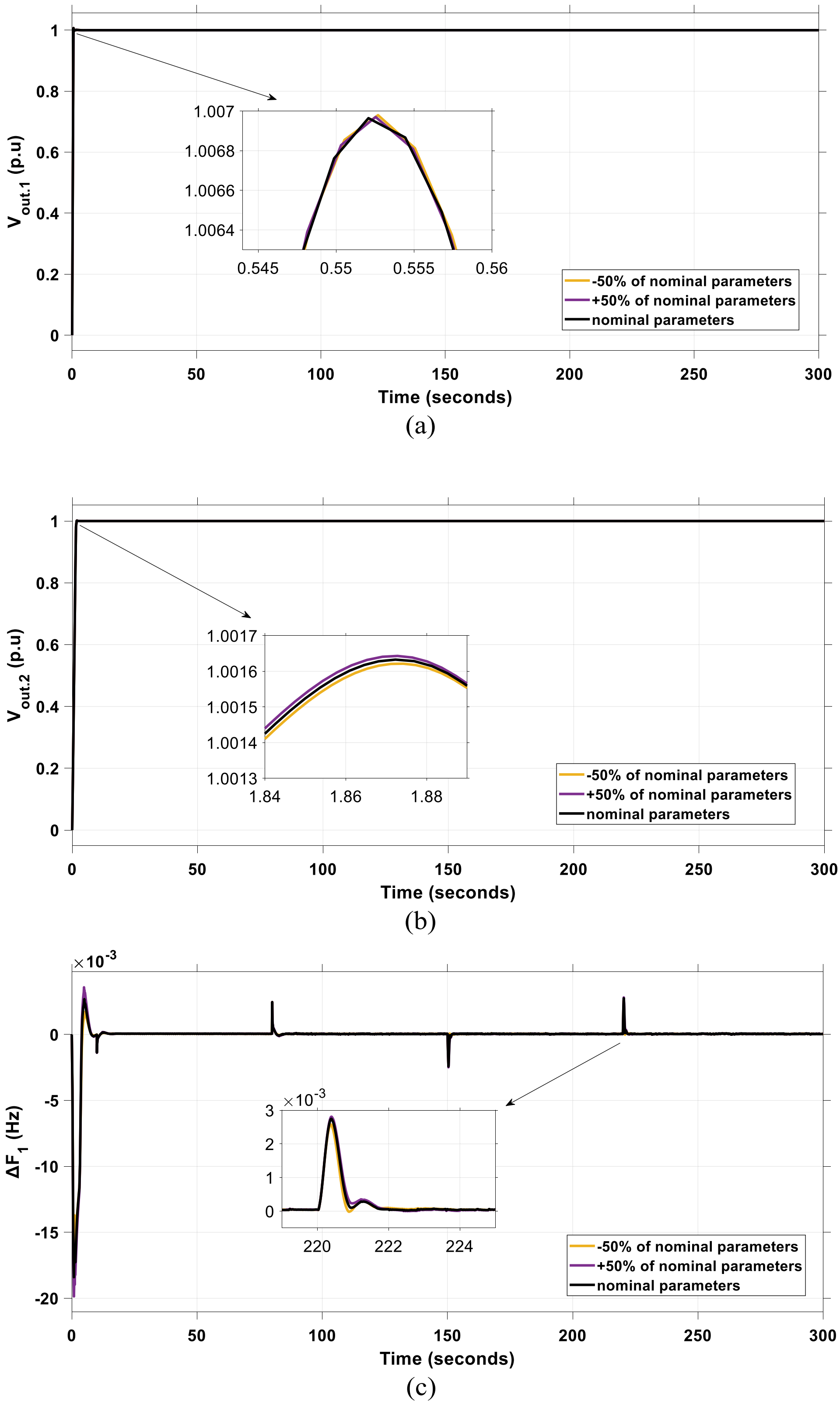

Fig. 33. Dynamic power system response for Case IV with a ±50% change in the system settings - (a) Vout1, (b) Vout2, (c) ⊿F1, (d) ⊿F2, (e) ⊿Ptie.

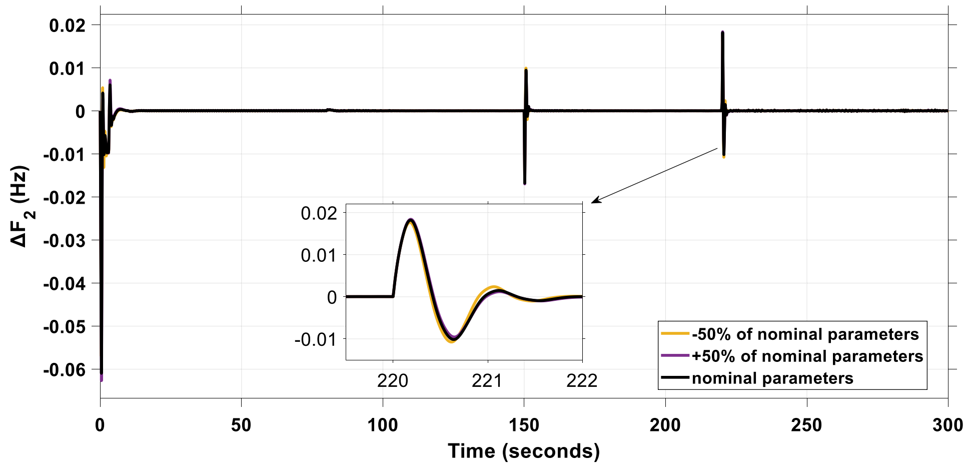

(d)

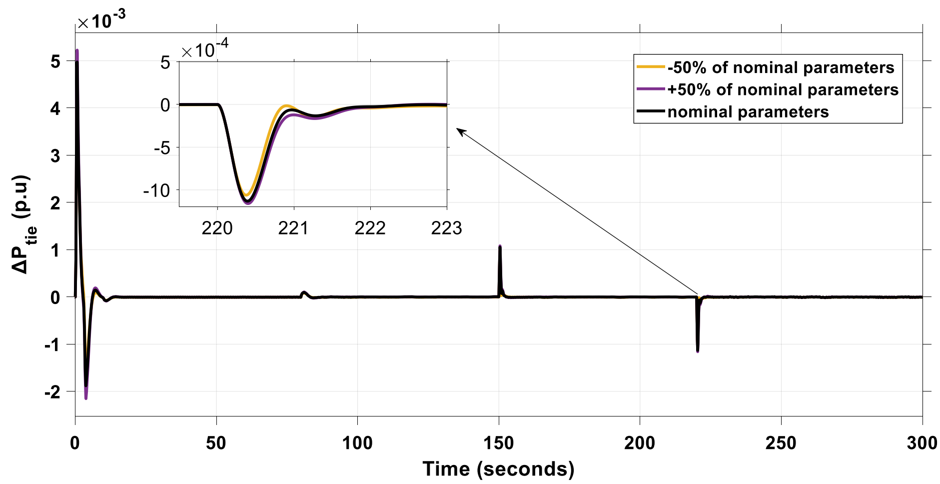

(e)

Fig. 33. (*continued*).

References

Abdollahzadeh, B., Soleimanian Gharehchopogh, F., Mirjalili, S., 2021. Artificial gorilla troops optimizer: a new nature-inspired metaheuristic algorithm for global optimization problems. Int. J. Intell. Syst. 36, 5887–5958.

Ahmadianfar, I., Bozorg-Haddad, O., Chu, X., 2020. Gradient-based optimizer: A new metaheuristic optimization algorithm. Inf. Sci. (NY) 540, 131–159. http://dx.doi.org/10.1016/j.ins.2020.06.037.

Ahmed, M., Magdy, G., Khamies, M., Kamel, S., 2022. Modified TID controller for load frequency control of a two-area interconnected diverse-unit power system. Int. J. Electr. Power Energy Syst. 135, 107528. http://dx.doi.org/10.1016/j.ijepes.2021.107528.

Al-Hinai, A., Alyammahi, H., Haes Alhelou, H., 2021. Coordinated intelligent frequency control incorporating battery energy storage system, minimum variable contribution of demand response, and variable load damping coefficient in isolated power systems. Energy Rep. 7, 8030–8041. http://dx.doi.org/10.1016/j.egyr.2021.07.072.

Barisal, A.K., Mishra, S., 2018. Improved PSO based automatic generation control of multi-source nonlinear power systems interconnected by AC/DC links. Cogent Eng. 5, 1422228. http://dx.doi.org/10.1080/23311916.2017.1422228.

Bhateshvar, Y.K., Mathur, H.D., Siguerdidjane, H., Bansal, R.C., 2017. Ant colony optimized fuzzy control solution for frequency oscillation suppression. Electr. Power Compon. Syst. 45, 1573–1584. http://dx.doi.org/10.1080/15325008.2017.1362073.

Bingul, Z., Karahan, O., 2018. A novel performance criterion approach to optimum design of PID controller using cuckoo search algorithm for AVR system. J. Franklin Inst. 355, 5534–5559. http://dx.doi.org/10.1016/j.jfranklin.2018.05.056.

Cam, E., Gorel, G., Mamur, H., 2017. Use of the genetic algorithm-based fuzzy logic controller for load-frequency control in a two area interconnected power system. Appl. Sci. (Basel) 7, 308. http://dx.doi.org/10.3390/app7030308.

Chatterjee, S., Mukherjee, V., 2016. PID controller for automatic voltage regulator using teaching–learning based optimization technique. Int. J. Electr. Power Energy Syst. 77, 418–429. http://dx.doi.org/10.1016/j.ijepes.2015.11.010.

Dhanasekaran, B., Siddhan, S., Kaliannan, J., 2020. Ant colony optimization technique tuned controller for frequency regulation of single area nuclear power generating system. Microprocess Microsyst. 73, 102953. http://dx.doi.org/10.1016/j.micpro.2019.102953.

Dhillon, S.S., Lather, J.S., Marwaha, S., 2016. Multi objective load frequency control using hybrid bacterial foraging and particle swarm optimized PI controller. Int. J. Electr. Power Energy Syst. 79, 196–209.

Ekinci, S., Hekimoğlu, B., 2019. Improved kidney-inspired algorithm approach for tuning of PID controller in AVR system. IEEE Access 7, 39935–39947.

Elkasem, A.H., Khamies, M., Magdy, G., Taha, I.B., Kamel, S., 2021. Frequency stability of AC/DC interconnected power systems with wind energy using arithmetic optimization algorithm-based fuzzy-PID controller. Sustainability 13, 12095.

Elmelegi, A., Mohamed, E.A., Aly, M., Ahmed, E.M., Mohamed, A.-A.A., Elbaksawi, O., 2021. Optimized tilt fractional order cooperative controllers for preserving frequency stability in renewable energy-based power systems. IEEE Access 9, 8261–8277. http://dx.doi.org/10.1109/access.2021.30497.

Fosha, C., Elgerd, O., 1970. The megawatt-frequency control problem: A new approach via optimal control theory. IEEE Trans. Power Appar. Syst. PAS-89, 563. http://dx.doi.org/10.1109/tpas.1970.292603.

Gaing, Z.L., 2004. A particle swarm optimization approach for optimum design of PID controller in AVR system. IEEE Trans. Energy Convers. 19, 384–391.

Gozde, H., Taplamacioglu, M.C., 2011. Comparative performance analysis of artificial bee colony algorithm for automatic voltage regulator (AVR) system. J. Franklin Inst. B 348, 1927–1946.

Guha, D., Roy, P.K., Banerjee, S., 2016. Load frequency control of interconnected power system using grey wolf optimization. Swarm Evol. Comput. 27, 97–115. http://dx.doi.org/10.1016/j.swevo.2015.10.004.

Gupta, A., Chauhan, A., Khanna, R., 2014. Design of AVR and ALFC for single area power system including damping control. In: 2014 Recent Advances in Engineering and Computational Sciences. RAECS, IEEE.

Gupta, M., Srivastava, S., Gupta, J.R.P., 2016. A novel controller for model with combined LFC and AVR loops of single area power system. J. Inst. Eng. (India) Ser. B 97, 21–29. http://dx.doi.org/10.1007/s40031-014-0159-z.

Hakimuddin, N., Khosla, A., Garg, J.K., 2020. Centralized and decentralized AGC schemes in 2-area interconnected power system considering multi source power plants in each area. J. King Saud Univ. - Eng. Sci. 32, 123–132. http://dx.doi.org/10.1016/j.jksues.2018.07.003.

Hasanien, H.M., El-Fergany, A.A., 2019. Salp swarm algorithm-based optimal load frequency control of hybrid renewable power systems with communication delay and excitation cross-coupling effect. Electr. Power Syst. Res. 176, 105938.

Kalyan, C.N.S., 2021. UPFC and SMES based coordinated control strategy for simultaneous frequency and voltage stability of an interconnected power system. In: 2021 1st International Conference on Power Electronics and Energy. ICPEE, IEEE.

Kalyan, C.N.S., Goud, B.S., Reddy, C.R., Bajaj, M., Sharma, N.K., Alhelou, H.H., Siano, P., Kamel, S., 2022. Comparative performance assessment of different energy storage devices in combined LFC and AVR analysis of multi-area power system. Energies 15 (2), 629.

Kalyan, C.H.N.S., Rao, G.S., 2021a. Demonstrating the effect of excitation cross coupling and communication time delays on automatic generation control. In: 2021 4th Biennial International Conference on Nascent Technologies in Engineering. ICNTE, IEEE, pp. 1–6.

Kalyan, C.H., Rao, G.S., 2021b. Impact of communication time delays on combined LFC and AVR of a multi-area hybrid system with IPFC-RFBs coordinated control strategy. Prot. Control Modern Power Syst. 6, 1–20.

Kalyan, C.N.S., Suresh, C.V., 2021. PIDD controller for AGC of nonlinear system with PEV integration and AC-DC links. In: 2021 International Conference on Sustainable Energy and Future Electric Transportation. SEFET, IEEE.

Khamari, D., Kumbhakar, B., Patra, S., Laxmi, D.A., Panigrahi, S., 2020. Load frequency control of a single area power system using firefly algorithm. Int. J. Eng. Res. 9.

Khishe, M., Mosavi, M.R., 2020. Chimp optimization algorithm. Expert Syst. Appl. 149, 113338.

Khudhair, M., Ragab, M., AboRas, K.M., Abbasy, N.H., 2022. Robust control of frequency variations for a multi-area power system in smart grid using a newly wild horse optimized combination of PIDD2 and PD controllers. Sustainability 14, 8223.

Kumar, V., Sharma, V., Naresh, R., 2021. HHO-based model predictive controller for combined voltage and frequency control problem including SMES. IETE J. Res. 1–15. http://dx.doi.org/10.1080/03772063.2021.1908180.

Lal, D.K., Barisal, A.K., 2019. Combined load frequency and terminal voltage control of power systems using moth flame optimization algorithm. J. Electr. Syst. Inf. Technol. 6. http://dx.doi.org/10.1186/s43067-019-0010-3.

Madasu, S.D., Sai Kumar, M.L.S., Singh, A.K., 2018. A flower pollination algorithm based automatic generation control of interconnected power system. Ain Shams Eng. J. 9, 1215–1224. http://dx.doi.org/10.1016/j.asej.2016.06.003.

Mirjalili, S., Lewis, A., 2016. The whale optimization algorithm. Adv. Eng. Softw. 95, 51–67.

Modabbernia, M., Alizadeh, B., Sahab, A., Moghaddam, M.M., 2020. Robust control of automatic voltage regulator (AVR) with real structured parametric uncertainties based on H∞ and μ-analysis. ISA Trans. 100, 46–62. http://dx.doi.org/10.1016/j.isatra.2020.01.010.

Mohanty, B., Hota, P.K., 2018. A hybrid chemical reaction-particle swarm optimisation technique for automatic generation control. J. Electr. Syst. Inf. Technol. 5, 229–244. http://dx.doi.org/10.1016/j.jesit.2017.04.001.

Morsali, J., Esmaeili, Z., 2020. Proposing a new hybrid model for LFC and AVR loops to improve effectively frequency stability using coordinative CPSS. In: 2020 28th Iranian Conference on Electrical Engineering. ICEE, IEEE.

Morsali, J., Zare, K., Tarafdar Hagh, M., 2018. Comparative performance evaluation of fractional order controllers in LFC of two-area diverse-unit power system with considering GDB and GRC effects. J. Electr. Syst. Inf. Technol. 5, 708–722. http://dx.doi.org/10.1016/j.jesit.2017.05.002.

Nahas, N., Abouheaf, M., Darghouth, M.N., Sharaf, A., 2021. A multi-objective AVR-lfc optimization scheme for multi-area power systems. Electr. Power Syst. Res. 200, 107467. http://dx.doi.org/10.1016/j.epsr.2021.107467.

Nahas, N., Abouheaf, M., Sharaf, A., Gueaieb, W., 2019. A self-adjusting adaptive AVR-LFC scheme for synchronous generators. IEEE Trans. Power Syst. 34, 5073–5075. http://dx.doi.org/10.1109/tpwrs.2019.2920782.

Nahas, N., Nourelfath, M., 2014. Nonlinear threshold accepting meta-heuristic for combinatorial optimisation problems. Int. J. Metaheuristics 3, 265. http://dx.doi.org/10.1504/ijmheur.2014.068904.

Ortiz-Quisbert, M.E., Duarte-Mermoud, M.A., Milla, F., Castro-Linares, R., Lefranc, G., 2018. Optimal fractional order adaptive controllers for AVR applications. Electr. Eng. (Berl, Print) 100, 267–283. http://dx.doi.org/10.1007/s00202-016-0502-2.

Rajbongshi, R., Saikia, L.C., 2017a. Combined control of voltage and frequency of multi-area multisource system incorporating solar thermal power plant using LSA optimised classical controllers. IET Gener. Transm. Distrib. 11, 2489–2498. http://dx.doi.org/10.1049/iet-gtd.2016.1154.

Rajbongshi, R., Saikia, L.C., 2017b. Combined control of voltage and frequency of multi-area multisource system incorporating solar thermal power plant using LSA optimised classical controllers. IET Gener. Transm. Distrib. 11, 2489–2498.

Rajbongshi, R., Saikia, L.C., 2019. Performance of coordinated interline power flow controller and power system stabilizer in combined multiarea restructured ALFC and AVR system. Int. Trans. Electr. Energy Syst. 29, e2822. http://dx.doi.org/10.1002/2050-7038.2822.

Rajbongshi, R., Saikia, L.C., Tasnin, W., Saha, A., Saha, D., 2018. Performance analysis of combined ALFC and AVR system incorporating power system stabilizer. In: 2018 2nd International Conference on Power, Energy and Environment: Towards Smart Technology. ICEPE, IEEE.

Rajesh, K.S., Dash, S.S., Rajagopal, R., 2019. Hybrid improved firefly-pattern search optimized fuzzy aided PID controller for automatic generation control of power systems with multi-type generations. Swarm Evol. Comput. 44, 200–211. http://dx.doi.org/10.1016/j.swevo.2018.03.005.

Rakhshani, E., Rouzbehi, K., Sadeh, S., 2009. A new combined model for simulation of mutual effects between LFC and AVR loops. In: 2009 Asia-Pacific Power and Energy Engineering Conference. IEEE.

Ranjan, S., Latif, A., Das, D.C., Sinha, N., Hussain, S.M.S., Ustun, T.S., Iqbal, A., 2021. Simultaneous analysis of frequency and voltage control of the interconnected hybrid power system in presence of FACTS devices and demand response scheme. Energy Rep. 7, 7445–7459. http://dx.doi.org/10.1016/j.egyr.2021.10.100.

Rao, G.S., 2020. Performance comparison of various energy storage devices in combined LFC and AVR of multi area system with renewable energy integration. Int. J. Renew. Energy Res. (IJRER) 10, 933–944.

Saadat, H., 2011. Power System Analysis, third ed. Psa Pub.

Shyama, T.R., Kumar, R.S., Shanmugasundaram, V., 2012. Design of FGSPI controller based combined LFC and AVR of two area interconnected power generating system. Int. J. Eng. Adv. Technol. 1, 135–139.

SinghParmar, P.K., Majhi, S.P., Kothari, D., 2012. LFC of an interconnected power system with thyristor controlled phase shifter in the tie line. Int. J. Comput. Appl. 41, 27–30.

Soundarrajan, A., Sumathi, S., Sundar, C., 2010. Particle swarm optimization based LFC and AVR of autonomous power generating system. IAENG Int. J. Comput. Sci. 37, 37, 1.

Tasnin, W., Saikia, L.C., 2018. Comparative performance of different energy storage devices in AGC of multi-source system including geothermal power plant. J. Renew. Sustain. Energy 10, 024101.

Topno, P.N., Chanana, S., 2018. Differential evolution algorithm based tilt integral derivative control for LFC problem of an interconnected hydro-thermal power system. J. Vib. Control 24, 3952–3973. http://dx.doi.org/10.1177/1077546317717866.

Tungadio, D.H., Sun, Y., 2019. Load frequency controllers considering renewable energy integration in power system. Energy Rep. 5, 436–453. http://dx.doi.org/10.1016/j.egyr.2019.04.003.

Vijaya Chandrakala, K.R.M., Balamurugan, S., 2016. Simulated annealing based optimal frequency and terminal voltage control of multi source multi area system. Int. J. Electr. Power Energy Syst. 78, 823–829. http://dx.doi.org/10.1016/j.ijepes.2015.12.026.

Yakout, A.H., Kotb, H., Hasanien, H.M., Aboras, K.M., 2021. Optimal fuzzy PIDF load frequency controller for hybrid microgrid system using marine predator algorithm. IEEE Access 9, 54220–54232. http://dx.doi.org/10.1109/access.2021.3070076.

Yogendra, A., 2018. Improvement in automatic generation control of two-area electric power systems via a new fuzzy aided optimal PIDN-FOI controller. ISA Trans. 80, 475–490. http://dx.doi.org/10.1016/j.isatra.2018.07.028.